

# COMPATIBLE FINITE ELEMENT INTERPOLATED NEURAL NETWORKS

SANTIAGO BADIA<sup>1</sup>, WEI LI<sup>1,\*</sup>, AND ALBERTO F. MARTÍN<sup>2</sup>

**ABSTRACT.** We extend the finite element interpolated neural network (FEINN) framework from partial differential equations (PDEs) with weak solutions in  $H^1$  to PDEs with weak solutions in  $H(\mathbf{curl})$  or  $H(\mathbf{div})$ . To this end, we consider interpolation trial spaces that satisfy the de Rham Hilbert subcomplex, providing stable and structure-preserving neural network discretisations for a wide variety of PDEs. This approach, coined compatible FEINNs, has been used to accurately approximate the  $H(\mathbf{curl})$  inner product. We numerically observe that the trained network outperforms finite element solutions by several orders of magnitude for smooth analytical solutions. Furthermore, to showcase the versatility of the method, we demonstrate that compatible FEINNs achieve high accuracy in solving surface PDEs such as the Darcy equation on a sphere. Additionally, the framework can integrate adaptive mesh refinements to effectively solve problems with localised features. We use an adaptive training strategy to train the network on a sequence of progressively adapted meshes. Finally, we compare compatible FEINNs with the adjoint neural network method for solving inverse problems. We consider a one-loop algorithm that trains the neural networks for unknowns and missing parameters using a loss function that includes PDE residual and data misfit terms. The algorithm is applied to identify space-varying physical parameters for the  $H(\mathbf{curl})$  model problem from partial, noisy, or boundary observations. We find that compatible FEINNs achieve accuracy and robustness comparable to, if not exceeding, the adjoint method in these scenarios.

## 1. INTRODUCTION

Conventional numerical discretisations of partial differential equations (PDEs) rely on a partition of the domain (mesh) to approximate a continuous problem. The most widely used discretisation methods are the finite element method (FEM), the finite difference method (FDM), and the finite volume method (FVM). Among these, FEM is very popular due to its flexibility to handle complex geometries, ability to achieve high-order accuracy, and suitability to tackle mixed formulations. Additionally, it is supported by a solid mathematical foundation [1], ensuring stability and accuracy. Over the past few decades, optimal FEM solvers for both linear and nonlinear PDEs have been developed, effectively exploiting the capabilities of large-scale supercomputers [2].

Various physical phenomena in science and engineering can be modelled using PDEs. As a classical example, the Poisson equation, with weak solution in  $H^1$ , describes phenomena such as heat conduction. The Maxwell's equations, with weak solution in  $H(\mathbf{curl})$ , succinctly state the fundamentals of electricity and magnetism, while the Darcy equation, with weak flux and pressure solution in  $H(\mathbf{div})$  and  $L^2$  spaces, respectively, describes fluid flow through porous media. These spaces are connected through the differential operators grad, curl, and div, such that applying an operator to functions in one space maps surjectively onto the kernel of the next operator in the sequence, thereby forming a de Rham complex [3].

Compatible finite elements (FEs) are structure-preserving discretisation methods for solving these equations. They search for approximate solutions in subspaces that, at the discrete level, preserve the same relation via differential operators as their continuous, infinite-dimensional counterparts, thus forming a discrete de Rham complex. A common property of these complexes is the gradual reduction of inter-element continuity requirements from one space to the next: the discrete subspaces are made of piecewise polynomials that are continuous across cell boundaries in the case of  $H^1$  (thus having a well defined global weak gradient), only tangential or only normal components are continuous for  $H(\mathbf{curl})$  and  $H(\mathbf{div})$ , respectively (thus having well-defined global weak curl and div, respectively), and completely discontinuous

<sup>1</sup> SCHOOL OF MATHEMATICS, MONASH UNIVERSITY, CLAYTON, VICTORIA 3800, AUSTRALIA.

<sup>2</sup> SCHOOL OF COMPUTING, THE AUSTRALIAN NATIONAL UNIVERSITY, CANBERRA ACT 2600, AUSTRALIA.

\* CORRESPONDING AUTHOR.

*E-mail addresses:* santiago.badia@monash.edu, wei.li@monash.edu, alberto.f.martin@anu.edu.au.

*Date:* March 17, 2025.

*Key words and phrases.* neural networks, PINNs, compatible finite elements, PDE approximation, surface PDEs, inverse problems.

across cell boundaries for  $L^2$ . Although quite established in several application areas, compatible FEs have become increasingly popular, e.g., for the simulation of geophysical flows in the context of atmospheric and ocean modelling, mostly because their ability to effectively address the issue of spurious numerical waves present in other numerical schemes, while allowing for conservation of energy and other quantities; see [4] for a recent survey.

For a given polytope (e.g., a triangle or a quadrilateral) and polynomial order, there are several possible choices for the discrete subspaces that lead to the above discrete complex structure. In this work we leverage first-kind Nédélec [5] and Raviart-Thomas (RT) [6] vector-valued FEs for  $H(\mathbf{curl})$  and  $H(\mathbf{div})$  spaces, respectively (apart from the more standard continuous and discontinuous Lagrangian nodal FEs for  $H^1$  and  $L^2$  spaces, respectively). These FEs define the local polynomial bases and degrees of freedom (DoFs) in the form of integrals (moments) over mesh edges, faces, and cells so as to ensure the above mentioned continuity constraints across element boundaries. We note that Nédélec FEs are particularly well-suited for Maxwell’s equations as, in contrast to nodal FEs, they avoid spurious solutions, even in the case of domains with re-entrant corners or edges [7]. They can accurately approximate discontinuous fields due to large jumps in the physical properties of the material, and are better understood mathematically than other discretisation methods for the Maxwell’s equations [8].

Deep learning techniques, especially neural networks (NNs), have gained significant popularity over the last few years for solving PDEs. The main idea is that one seeks an approximation to the solution of a PDE from a trial finite-dimensional *nonlinear manifold* (e.g., a neural network) as opposed to a finite-dimensional linear space as in FEM. One of the most notable methods is physics-informed NNs (PINNs) [9]. Instead of solving algebraic systems of equations to find an approximate solution, PINNs minimise the strong PDE residual evaluated at a set of randomly sampled collocation points. PINNs have demonstrated relative success for forward (where only the solution/state is unknown) and inverse (where incomplete data, e.g., physical coefficients, is supplemented with observations of the state) PDE-constrained problems (see, e.g., [10, 11]).

The variational PINN (VPINN) method [12] utilises a loss function based on the variational or weak form of the PDE in order to weaken the regularity requirements on the solution. VPINNs support  $h$ -refinement through domain decomposition and  $p$ -refinement via projection onto higher-order polynomial spaces. One of the issues in VPINNs and PINNs is the difficulties associated to the accurate integration of NNs (and their derivatives) [13]. To address the integration challenge in VPINNs, the interpolated VPINN (IVPINN) method [14] proposes using polynomial interpolations of NNs as trial functions in the variational formulation. IVPINNs reduce computational costs compared to VPINNs and demonstrate significantly higher accuracy, especially when the solution is singular. Despite the improvements, these variational methods make use of the Euclidean norm of the discrete residual, which is not an appropriate measure of the error, since the residual is a functional in the dual space. As a result, the analysis for IVPINNs is sub-optimal.

Another challenge in PINN-based methods is the imposition of essential boundary conditions [15]. These methods either impose the boundary conditions weakly through a penalty term [9] or Nitsche’s method [13], or rely on a combination of two functions: an offset function that satisfies the boundary conditions and a distance function that vanishes at the boundary [14].

On the other hand, the so-called FE interpolated NN (FEINN) method, proposed in [16], aims to find a function among all possible realisations of the nonlinear NN manifold whose interpolation onto a trial FE space minimises a discrete dual norm, over a suitable test FE space, of the weak residual functional associated to the PDE. The FEINN method imposes essential boundary conditions more naturally at the FE space level by interpolating the NNs onto a FE space that (approximately) satisfies the Dirichlet boundary conditions. The integration of the loss function can efficiently be handled using a Gaussian quadrature, as in FEM. The dual norm of the residual is an accurate measure of the error and the analysis in [16] shows that the interpolation of the NNs onto the FE space is a stable and accurate approximation of the solution. We refer to [17] for the use of the dual norm of the residual in VPINNs.

FEINNs have demonstrated exceptional performance over FEM when the target solution is smooth: the trained NNs outperform FEM solutions by several orders of magnitude in terms of  $L^2$  and  $H^1$  errors, even with complex geometries. With minimal modifications, FEINNs can also be extended to solve inverse problems and exhibit comparable performance to the adjoint-based NN approach [16]. Besides, when combined with adaptive meshing techniques,  $h$ -adaptive FEINNs [18] can efficiently solve PDEs featuring sharp gradients and singularities while unlocking the nonlinear approximation power of discrete NN

manifold spaces. The trained NNs show potential to achieve higher accuracy than FEM, particularly when the solution is not singular [18].

Most existing NN discretisation PDE solvers are developed for problems with weak solutions in  $H^1$ , such as the Poisson equation [13, 18], or in  $H^1 \times L^2$ , such as the Navier-Stokes equations [19–21]. However, there are limited studies attacking problems with weak solutions in  $H(\mathbf{curl})$  or  $H(\mathbf{div})$ . In [22], the authors employ NNs to solve 1D nonlinear magneto quasi-static Maxwell’s equations in frequency or time domains. Similar to PINNs, MaxwellNet [23] trains a convolutional NN (CNN) using the strong PDE residual of the Maxwell’s equations as the loss function. The authors in [24] address inverse Maxwell’s problems by integrating a hypernetwork into the PINN framework. This addition enables the trained hypernetwork to act as a parametrised real-time field solver, allowing rapid solutions to inverse electromagnetic problems.

There are even fewer works on NN-based solvers for the Darcy equation. The physics-informed CNN (PICNN) method proposed in [25] uses a CNN to simulate transient two-phase Darcy flows in homogeneous and heterogeneous reservoirs. To ensure flux continuity, they adopt a FVM to approximate the PDE residual in the loss function. In [26], the authors employ multiple NNs to approximate both the unknown parameters and states of the inverse Darcy systems. Their study shows that PINNs offer regularisation and decrease the uncertainty in NN predictions.

Another interesting topic is the development of NN solvers for PDEs posed over immersed manifolds, e.g., the Darcy equation defined on a sphere. There are a few works on PINNs for surface PDEs in the literature. In [27], the authors extend PINNs to solve the Laplace-Beltrami equation on 3D surfaces. The authors in [28] utilise a single-hidden-layer PINNs to solve the Laplace-Beltrami and time-dependent diffusion equations on static surfaces, as well as advection-diffusion equations on evolving surfaces. Another related work is [29], where the authors apply PINNs to solve the shallow-water equations on the sphere.

In this work, we integrate compatible FEs, i.e., spaces that form a discrete the Rham complex [3], into the FEINN method proposed in [16]. This integration enables us to solve PDEs with weak solutions in  $H(\mathbf{curl})$  or  $H(\mathbf{div})$ . We refer to this method as compatible FEINNs. The novelty of compatible FEINNs over the standard FEINN method in [16] lies in introducing curl/div-conforming trial FE spaces to interpolate NNs, ensuring the desired structure-preserving properties across element boundaries. The residual minimisation framework underlying FEINNs allows for some flexibility in selecting the trial and test FE spaces provided that an inf-sup compatibility condition is satisfied among them; see [18] for the numerical analysis of the method. As we showed in [16] and further confirmed in this paper for the problems at hand, a proper choice of these spaces can lead to significant improvements in the accuracy of the solution and the convergence of the optimiser. As an evidence on the soundness of this approach, we also showcase its applicability to solve PDEs posed over immersed manifolds. We interpolate NN vector-valued fields living in ambient space (and thus not necessarily tangent to the manifold) onto FE spaces made of functions constrained to be tangent to the manifold by construction. Strikingly, NNs trained on a coarse mesh and lower-order bases are able to provide several orders of magnitude higher accurate solutions to the problem when interpolated onto a FE space built out of finer meshes and higher order bases. Besides, this method, which resembles TraceFEM [30] (as it seeks an approximation of the surface PDE on a finite-dimensional space of functions living on a higher dimensional space), does not need stabilisation terms in the loss function to enforce tangentiality, as it relies on a surface FE interpolation on the tangent space. A comprehensive set of numerical experiments is conducted to demonstrate the performance of compatible FEINNs in forward and inverse problems involving PDEs in  $H(\mathbf{curl})$  and  $H(\mathbf{div})$ .

The rest of the paper is organised as follows. In Sect. 2, we introduce model problems for the Maxwell’s equations and Darcy equation considered in this article, their compatible FE discretisation, and the compatible FEINN method in both forward and inverse scenarios. Sect. 3 starts with a brief discussion on the implementation, and then presents the numerical results of the forward and inverse experiments. Finally, we conclude the paper in Sect. 4.

## 2. METHODOLOGY

**2.1. Notation.** In this section we introduce some essential mathematical notation that will be required for the rest of the paper. Let  $\Omega \subset \mathbb{R}^d$  be a Lipschitz polyhedral domain, where  $d \in \{2, 3\}$  is the dimension of the space where  $\Omega$  lives. We denote the boundary of  $\Omega$  by  $\partial\Omega$ , the Dirichlet boundary by  $\Gamma_D \subset \partial\Omega$ , and the Neumann boundary by  $\Gamma_N \subset \partial\Omega$ . Note that  $\Gamma_D \cup \Gamma_N = \partial\Omega$  and  $\Gamma_D \cap \Gamma_N = \emptyset$ . We consider a scalar-valued function  $p : \Omega \rightarrow \mathbb{R}$ , a vector-valued function  $\mathbf{u} : \Omega \rightarrow \mathbb{R}^d$ , and the standard square-integrable

spaces  $L^2(\Omega)$  for scalar functions and  $L^2(\Omega)^d$  for vector functions. The corresponding norms are denoted by  $\|\cdot\|_{L^2(\Omega)}$  and  $\|\cdot\|_{L^2(\Omega)^d}$ , respectively.

In three dimensions ( $d = 3$ ), we have the following spaces:

$$\begin{aligned} H^1(\Omega) &= \{p \in L^2(\Omega) : \nabla p \in L^2(\Omega)^d\}, \\ H(\mathbf{curl}; \Omega) &= \{\mathbf{u} \in L^2(\Omega)^d : \nabla \times \mathbf{u} \in L^2(\Omega)^d\}, \\ H(\mathbf{div}; \Omega) &= \{\mathbf{u} \in L^2(\Omega)^d : \nabla \cdot \mathbf{u} \in L^2(\Omega)\}, \end{aligned}$$

where  $\nabla$ ,  $\nabla \times$ ,  $\nabla \cdot$  denote the weak gradient, curl, and divergence differential operators, respectively. Detailed definitions of these spaces and operators can be found in, e.g., [1]. We equip these spaces with the following norms:

$$\begin{aligned} \|p\|_{H^1(\Omega)} &= \left( \|p\|_{L^2(\Omega)}^2 + \|\nabla p\|_{L^2(\Omega)^d}^2 \right)^{1/2}, \\ \|\mathbf{u}\|_{H(\mathbf{curl}; \Omega)} &= \left( \|\mathbf{u}\|_{L^2(\Omega)^d}^2 + \|\nabla \times \mathbf{u}\|_{L^2(\Omega)^d}^2 \right)^{1/2}, \\ \|\mathbf{u}\|_{H(\mathbf{div}; \Omega)} &= \left( \|\mathbf{u}\|_{L^2(\Omega)^d}^2 + \|\nabla \cdot \mathbf{u}\|_{L^2(\Omega)}^2 \right)^{1/2}. \end{aligned}$$

In two dimensions ( $d = 2$ ), the curl operator is defined as the divergence of a 90 degrees counter-clockwise rotation of the input vector, and thus produces scalar functions (as opposed to vector-valued functions for  $d = 3$ ). Thus, for the curl case, we have for  $d = 2$ :

$$H(\mathbf{curl}; \Omega) = \{\mathbf{u} \in L^2(\Omega)^2 : \nabla \times \mathbf{u} \in L^2(\Omega)\}, \quad \|\mathbf{u}\|_{H(\mathbf{curl}; \Omega)} = \left( \|\mathbf{u}\|_{L^2(\Omega)^d}^2 + \|\nabla \times \mathbf{u}\|_{L^2(\Omega)}^2 \right)^{1/2}.$$

**2.2. Continuous problems.** As model problems, we consider two types of PDEs: the inner product in  $H(\mathbf{curl})$  on a  $d$ -dimensional domain (as a simplified model problem for the Maxwell's equations) and the Darcy equation defined on a 2-dimensional closed surface (i.e., manifold) embedded in 3-dimensional space. In the following, we denote the  $H(\mathbf{curl})$  problem as the Maxwell problem for brevity, even though it is a simplification of the full Maxwell's system.

**2.2.1. Maxwell's equations.** As a model problem for the Maxwell's equations, we consider the  $H(\mathbf{curl})$ -inner product problem: find the field  $\mathbf{u} : \Omega \rightarrow \mathbb{R}^d$  such that

$$\nabla \times \nabla \times \mathbf{u} + \kappa \mathbf{u} = \mathbf{f} \text{ in } \Omega, \quad \mathbf{u} \times \mathbf{n} = \mathbf{g} \text{ on } \Gamma_D = \partial\Omega, \quad (1)$$

where  $\kappa$  is a scalar-valued material parameter field,  $\mathbf{f}$  is a source term,  $\mathbf{n}$  is the outward unit normal vector to  $\partial\Omega$ , and  $\mathbf{g}$  is the Dirichlet data. Note that, for simplicity and without loss of generality, we consider pure Dirichlet boundary conditions (i.e.,  $\Gamma_N = \emptyset$ ). Imposition of Neumann boundary conditions is straightforward and can be included in the formulation by a simple modification of the right-hand side (RHS).

Let  $U^1 \doteq H(\mathbf{curl}; \Omega)$  and its subspace  $U_0^1 \doteq \{\mathbf{v} \in H(\mathbf{curl}; \Omega) : \mathbf{v} \times \mathbf{n} = 0 \text{ on } \partial\Omega\}$ . Consider the bilinear and linear forms:

$$a(\mathbf{u}, \mathbf{v}) = \int_{\Omega} (\nabla \times \mathbf{u}) \cdot (\nabla \times \mathbf{v}) + \kappa \mathbf{u} \cdot \mathbf{v}, \quad \ell(\mathbf{v}) = \int_{\Omega} \mathbf{f} \cdot \mathbf{v}.$$

The weak form of (1) reads: find the solution  $\mathbf{u} + \bar{\mathbf{u}} \in U^1$ , with  $\mathbf{u} \in U_0^1$  such that

$$a(\mathbf{u}, \mathbf{v}) = \ell(\mathbf{v}) - a(\bar{\mathbf{u}}, \mathbf{v}), \quad \forall \mathbf{v} \in U_0^1, \quad (2)$$

and  $\bar{\mathbf{u}}$  an offset (a.k.a. lifting) function satisfying the Dirichlet boundary conditions. The well-posedness of this problem can be proven invoking the Lax-Milgram lemma [31]. We also define the weak PDE residual functional for the problem as

$$\mathcal{R}(\mathbf{u}) = a(\mathbf{u} + \bar{\mathbf{u}}, \cdot) - \ell(\cdot) \in U_0^1', \quad (3)$$

where  $U_0^1'$  denotes the dual space of  $U_0^1$ .

2.2.2. *Darcy equation on a closed surface.* The strong form of the Darcy equations defined on a closed two-dimensional manifold  $S$  embedded in three dimensions read: find the flux  $\mathbf{u} : S \rightarrow \mathbb{R}^3$  and the pressure  $p : S \rightarrow \mathbb{R}$  such that

$$\nabla_S \cdot \mathbf{u} = f \text{ in } S, \quad \mathbf{u} = -\nabla_S p \text{ in } S, \quad (4)$$

where  $\nabla_S \cdot$  and  $\nabla_S$  denote the divergence and gradient operators on the manifold  $S$ , respectively. The vector-valued fields  $\mathbf{u}$  and  $\nabla_S p$  are, by definition, constrained to be tangent to  $S$ . Note that boundary conditions are not part of the system due to the closed nature of  $S$ .

We define the spaces  $U^2 \doteq H(\mathbf{div}; S)$ ,  $U^3 \doteq L^2(S)$  and  $\tilde{U}^3 \doteq L_0^2(S) \doteq \{q \in L^2(S) : \int_S q = 0\}$ . We denote  $(\cdot, \cdot)$  as the  $L^2(S)$  inner product, i.e.,  $(p, q) = \int_S p q$ . The weak form of (4) reads: find  $(\mathbf{u}, p) \in U^2 \times \tilde{U}^3$  such that

$$(\mathbf{u}, \mathbf{v}) - (p, \nabla_S \cdot \mathbf{v}) = 0 \quad \forall \mathbf{v} \in U^2, \quad (\nabla_S \cdot \mathbf{u}, q) = (f, q) \quad \forall q \in \tilde{U}^3, \quad (5)$$

or, equivalently, the mixed formulation:

$$\mathcal{A}((\mathbf{u}, \mathbf{v}), (p, q)) = \mathcal{L}((\mathbf{v}, q)) \quad \forall (\mathbf{v}, q) \in U^2 \times \tilde{U}^3, \quad (6)$$

with the mixed forms defined as

$$\mathcal{A}((\mathbf{u}, \mathbf{v}), (p, q)) \doteq (\mathbf{u}, \mathbf{v}) - (p, \nabla_S \cdot \mathbf{v}) + (\nabla_S \cdot \mathbf{u}, q), \quad \mathcal{L}((\mathbf{v}, q)) \doteq (f, q).$$

We can also define the weak PDE residual for this problem as

$$\mathcal{R}(\mathbf{u}, p) = \mathcal{A}((\mathbf{u}, p), (\cdot, \cdot)) - \mathcal{L}((\cdot, \cdot)) \in U^{2'} \times \tilde{U}^{3'}, \quad (7)$$

where  $U^{2'}$  and  $\tilde{U}^{3'}$  are the dual spaces of  $U^2$  and  $\tilde{U}^3$ , respectively. The well-posedness of this problem can be proven invoking the Babuška-Brezzi theory [31].

### 2.3. Finite element discretisation.

2.3.1. *Discrete de Rham complexes.* Compatible FE spaces form a discrete differential complex, namely a de Rham complex [1, 3]. These complexes comprise a sequence of spaces related by differential operators. For  $\Omega \subset \mathbb{R}^3$ , it reads as follows:

$$\begin{array}{ccccccc} U^0 = H^1(\Omega) & \xrightarrow{d^1=\nabla} & U^1 = H(\mathbf{curl}; \Omega) & \xrightarrow{d^2=\nabla \times} & U^2 = H(\mathbf{div}; \Omega) & \xrightarrow{d^3=\nabla \cdot} & U^3 = L^2(\Omega) \\ \downarrow \pi_h^0 & & \downarrow \pi_h^1 & & \downarrow \pi_h^2 & & \downarrow \pi_h^3 \\ U_h^0 & \xrightarrow{d^1=\nabla} & U_h^1 & \xrightarrow{d^2=\nabla \times} & U_h^2 & \xrightarrow{d^3=\nabla \cdot} & U_h^3. \end{array} \quad (8)$$

In the top row, we have the continuous spaces, and in the bottom row, we have the corresponding discrete subspaces, i.e.,  $U_h^i \subset U^i$ . The differential operators  $d^i$  map between the continuous spaces in such a way that the image of  $d^i$  is the kernel of  $d^{i+1}$ , i.e.,  $d^{i+1} \circ d^i = 0$  for  $i \in \{1, 2\}$ . This very same relation is preserved for the discrete spaces in the bottom row, forming a discrete de Rham complex. Besides, using suitable interpolation operators  $\pi_h^i$ ,  $i \in \{0, 1, 2, 3\}$ , both complexes are connected by commutative relations  $d^i \pi_h^{i-1} u = \pi_h^i d^i u$ ,  $i \in \{1, 2, 3\}$ . For  $d = 2$ , rotating any vector field in  $H(\mathbf{div}; \Omega)$  by  $\pi/2$  radians counter clock-wise results in a vector field in  $H(\mathbf{curl}; \Omega)$ . Therefore, the de Rham complex in two dimensions can be simplified by removing  $U^1$ ,  $\pi_h^1$ ,  $U_h^1$ , and  $d^2$  from (8) and applying a 90-degree counter-clockwise rotation to the output of the gradient operator.

2.3.2. *Edge and face finite elements.* In order to build  $U_h^1$  and  $U_h^2$  (see (8)) we leverage the Nédélec edge elements of the first kind [5] and the RT face elements [6], respectively, out of the different options available. These FEs are well-established in the literature. We thus refer the reader to, e.g., [1, 32] for a detailed definition of their building blocks. Let  $\mathcal{T}_h$  be a shape-regular partition of  $\Omega$  with element size  $h > 0$ . Let  $K$  be an arbitrary cell of  $\mathcal{T}_h$ . For  $k \geq 1$ , we denote by  $\mathbf{RT}_k(K)$  and  $\mathbf{ND}_k(K)$  the RT and Nédélec elements of the first kind of order  $k$ , respectively, on cell  $K$ . We have that:

$$\begin{aligned} U_h^1 &:= \{\mathbf{u}_h \in H(\mathbf{curl}; \Omega) : \mathbf{u}_h|_K \in \mathbf{ND}_k(K), \quad \forall K \in \mathcal{T}_h\}, \\ U_h^2 &:= \{\mathbf{x}_h \in H(\mathbf{div}; \Omega) : \mathbf{x}_h|_K \in \mathbf{RT}_k(K), \quad \forall K \in \mathcal{T}_h\}, \end{aligned}$$

with  $\pi_h^1$  and  $\pi_h^2$  in (8) being the global Nédélec and RT interpolators [1]. For example, for  $k = 1$  (i.e., lowest order), these interpolation operators involve the evaluation of DoFs defined as integrals over global mesh

faces and edges of the normal and tangential components, respectively, of the vector field to be interpolated into the global FE space.

**2.3.3. Linearised test spaces.** Following the observations in [18] for grad-conforming problems, we consider a Petrov-Galerkin discretisation method for the FE discretisation of the curl and div-conforming problems being considered in this work. We define  $V_h^i$  as the *linearised* test space corresponding to the trial space  $U_h^i$ . In the following, we discuss the construction of this linearised test space  $V_h^1$  for the Maxwell problem and  $V_h^2$  for the Darcy problem.

Let  $k_U$  denote the order of  $U_h^i$ , and let  $\mathcal{T}_{h/k_U}$  represent the mesh obtained by  $k_U - 1$  uniform refinements of  $\mathcal{T}_h$ . The test space  $V_h^i$  is constructed out of the lowest order elements on the refined mesh  $\mathcal{T}_{h/k_U}$ . For example,  $V_h^1$  and  $V_h^2$  are built out of the lowest order Nédélec and RT elements, respectively, on  $\mathcal{T}_{h/k_U}$ . For this reason, we refer to  $V_h^i$  as a *linearised* test FE space. In the following propositions, we show that the dimensions of  $U_h^i$  and  $V_h^i$  are equal for  $i \in \{1, 2\}$  in 2D and 3D, but the proof can readily be extended to any dimension and other compatible spaces [33]. The grad-conforming linearised space was studied in [16]. The result straightforwardly holds for  $U_h^3$ .

**Proposition 2.1.** *The trial space  $U_h^1$  and the linearised test space  $V_h^1$  for quadrilateral and hexahedral Nédélec elements of the first kind have the same number of DoFs per geometrical entity (edge, face, cell) on the mesh  $\mathcal{T}_h$  and as a result the same dimensions.*

*Proof.* Each quadrilateral Nédélec element of order  $k_U$  has a total of  $2k_U(k_U + 1)$  DoFs:  $4k_U$  on the boundary edges (with  $k_U$  DoFs per edge) and  $2k_U(k_U - 1)$  in the interior. After applying  $k_U - 1$  uniform refinements, the refined element contains  $4k_U$  boundary subedges and  $2k_U(k_U - 1)$  interior subedges. Since the lowest order Nédélec element has one DoF per edge, the linearised element has  $4k_U$  boundary DoFs and  $2k_U(k_U - 1)$  interior DoFs. Therefore, the DoFs per geometrical entity and dimensions of  $U_h^1$  and  $V_h^1$  are equal for quadrilateral Nédélec elements.

Each hexahedral Nédélec element of order  $k_U$  has a total of  $3k_U(k_U + 1)^2$  DoFs:  $12k_U$  on the edges (with  $k_U$  DoFs per edge),  $6(2k_U^2 - 2k_U)$  on the faces (with  $2k_U^2 - 2k_U$  DoFs per face), and  $3k_U(k_U - 1)^2$  in the interior. After applying  $k_U - 1$  uniform refinements, the refined element has  $k_U$  subedges on each of the original edges,  $2k_U^2 - 2k_U$  subedges on each of the original faces, and  $3k_U(k_U - 1)^2$  interior subedges. The linearised Nédélec element also has  $12k_U$  edge DoFs,  $6(2k_U^2 - 2k_U)$  face DoFs, and  $3k_U(k_U - 1)^2$  interior DoFs. Thus, the DoFs per geometrical entity and dimensions of  $U_h^1$  and  $V_h^1$  are also equal for hexahedral Nédélec elements.  $\square$

**Proposition 2.2.** *The trial space  $U_h^2$  and the linearised test space  $V_h^2$  for quadrilateral and hexahedral RT elements have the same number of DoF per geometrical entity (edge, face, cell) on the mesh  $\mathcal{T}_h$  and as a result the same dimensions.*

*Proof.* Since quadrilateral Nédélec elements can be built by rotating RT elements [1], Prop. 2.1 applies to quadrilateral RT elements as well. Thus, the DoFs per geometrical entity and the dimensions of  $U_h^2$  and  $V_h^2$  are equal for these 2D elements.

Each hexahedral RT element of order  $k_U$  has a total of  $3k_U^2(k_U + 1)$  DoFs:  $6k_U^2$  on the faces (with  $k_U^2$  DoFs per face) and  $3k_U^2(k_U - 1)$  in the interior. After applying  $k_U - 1$  uniform refinements, the refined element has  $k_U^2$  subfaces on each of the original faces and  $3k_U^2(k_U - 1)$  interior subfaces. Since the lowest order RT element has one DoF per face, the linearised RT element also has  $6k_U^2$  face DoFs and  $3k_U^2(k_U - 1)$  interior DoFs. Thus, the DoFs per geometrical entity and the dimensions of  $U_h^2$  and  $V_h^2$  are also equal for hexahedral RT elements.  $\square$

**2.3.4. Maxwell problem finite element discretisation.** Let us consider an offset  $\bar{\mathbf{u}}_h \in U_h^1$  such that  $\bar{\mathbf{u}}_h = \pi_h^1(\mathbf{g})$  on  $\Gamma_D$ . A common choice is to extend  $\bar{\mathbf{u}}_h$  by zero on the interior. We use the subscript 0 to denote the continuous and discrete spaces with zero trace on  $\partial\Omega$  and  $\pi_{h,0}^i$  to represent the interpolation onto these subspaces. For example,  $U_{h,0}^1$  is the discrete subspace of  $U_h^1$  with zero tangential trace on  $\partial\Omega$  and  $\pi_{h,0}^1 : U_0^1 \rightarrow U_{h,0}^1$ . With these ingredients, we can formulate the FE problem for the Maxwell's problem as: find  $\mathbf{u}_h \in U_{h,0}^1$  such that

$$a(\mathbf{u}_h, \mathbf{v}_h) = \ell(\mathbf{v}_h) - a(\bar{\mathbf{u}}_h, \mathbf{v}_h), \quad \forall \mathbf{v}_h \in V_{h,0}^1. \quad (9)$$

The FE residual for this problem is defined as

$$\mathcal{R}_h(\mathbf{u}_h) = a(\mathbf{u}_h + \bar{\mathbf{u}}_h, \cdot) - \ell(\cdot) \in V_{h,0}^1. \quad (10)$$

The well-posedness of the discrete problem depends on a inf-sup compatibility condition between the discrete spaces  $U_{h,0}^1$  and  $V_{h,0}^1$ .

**2.3.5. Surface Darcy problem finite element discretisation.** In this section, we consider the FE discretisation of the Darcy problem on a closed surface; the restriction to a flat space is straightforward. It relies on a discrete approximation of the manifold  $S$ , denoted by  $S_h$ . For the particular case  $S$  is a sphere, a common choice for the discrete manifold  $S_h$ , of particular relevance for computational atmospheric flow dynamics, is the so-called cubed-sphere mesh [34]. In this mesh,  $S_h$  is made of quadrilateral elements  $K \subset \mathbb{R}^3$  (thus living in 3D ambient space) that are the image under a diffeomorphism  $\Phi_K$  of a reference square  $\hat{K} \subset \mathbb{R}^2$ . That is, we have that  $K = \Phi_K(\hat{K})$ . We denote by  $J_K$  the Jacobian of  $\Phi_K$ , and stress that  $J_K$  has three rows and two columns (as  $\Phi_K$  has three components, and depends on two parameters). We use  $G_K = J_K^T J_K$  to denote the corresponding first fundamental form.

We pursue the approach in [35] to build the FE space  $U_h^2$  on  $S_h$ . This space is made of piece-wise polynomial vector-valued fields tangent to  $S_h$  with normal component continuous across element interfaces. To this end, this approach relies on a  $\mathbf{RT}_k(\hat{K})$  element defined on parametric space  $\hat{K}$ . Let  $\mathbf{u}_h$  be an arbitrary element of  $U_h^2$ , and  $\mathbf{u}_h|_K$  its restriction to  $K$ . Then the surface contravariant Piola mapping is applied to build  $\mathbf{u}_h|_K$  out of its pullback vector-valued function  $\hat{\mathbf{u}} \in \mathbf{RT}_k(\hat{K})$  in parametric space. Namely, we have that  $\mathbf{u}_h|_K \circ \Phi_K(\hat{\mathbf{x}}) = \frac{1}{\sqrt{|G_K|}} J_K \hat{\mathbf{u}}(\hat{\mathbf{x}})$ . We stress that  $\hat{\mathbf{u}} \in \mathbb{R}^2$  while  $\mathbf{u}_h|_K \in \mathbb{R}^3$ . A similar (but different) construction is used to compute the discrete surface divergence operator  $\nabla_{S_h} \cdot \mathbf{u}_h$  on each cell. We refer to [35] for further details.

As for the curl-conforming problem, we can also consider a Petrov-Galerkin discretisation of this problem using the linearised space  $V_h^i$  for  $i \in \{2, 3\}$  discussed above. With these ingredients, the Petrov-Galerkin discretisation of (4) reads as: find  $(\mathbf{u}_h, p_h) \in U_h^2 \times \tilde{U}_h^3$  such that

$$\mathcal{A}_h((\mathbf{u}_h, \mathbf{v}_h), (p_h, q_h)) = \mathcal{L}_h((\mathbf{v}_h, q_h)) \quad \forall (\mathbf{v}_h, q_h) \in V_h^2 \times V_h^3, \quad (11)$$

where  $\mathcal{A}_h$  and  $\mathcal{L}_h$  are the discrete mixed forms corresponding to  $\mathcal{A}$  and  $\mathcal{L}$ , respectively, and  $S$  is replaced by  $S_h$ , and  $\nabla_S \cdot$  is replaced by  $\nabla_{S_h} \cdot$ . We note that this problem, as-is, does not have a unique solution. Another solution can be obtained by adding an arbitrary constant to the discrete pressure field  $p_h$ . To fix the constant, we further impose the constraint  $\int_{S_h} p_h = 0$  using a Lagrange multiplier. This detail is omitted from the presentation for brevity. Besides, the FE residual for this problem is defined as

$$\mathcal{R}_h(\mathbf{u}_h, p_h) = \mathcal{A}((\mathbf{u}_h, p_h), \cdot) - \mathcal{L}(\cdot) \in V_h^{2'} \times V_h^{3'}. \quad (12)$$

The well-posedness of this saddle-point problem relies on the Babuska-Brezzi theory (see [31]).

**2.4. Neural networks.** We utilise fully-connected, feed-forward NNs composed of affine maps and nonlinear activation functions. We use a tuple  $(n_0, \dots, n_L) \in \mathbb{N}^{(L+1)}$  to represent the network architecture, where  $L$  is the number of layers, and  $n_k$  (for  $1 \leq k \leq L$ ) is the number of neurons at each layer. Clearly,  $n_0 = d$ ; for scalar-valued NNs,  $n_L = 1$ ; for vector-valued NNs,  $n_L = d$ . Following [16, 18], we adopt  $n_1 = n_2 = \dots = n_{L-1} = n$ , meaning all the hidden layers have an equal number of neurons  $n$ .

At each layer  $k$  (for  $1 \leq k \leq L$ ), we denote the affine map as  $\Theta_k : \mathbb{R}^{n_{k-1}} \rightarrow \mathbb{R}^{n_k}$ , defined by  $\Theta_k \mathbf{x} = \mathbf{W}_k \mathbf{x} + \mathbf{b}_k$ , where  $\mathbf{W}_k \in \mathbb{R}^{n_k \times n_{k-1}}$  is the weight matrix and  $\mathbf{b}_k \in \mathbb{R}^{n_k}$  is the bias vector. After each affine map except the final one, we apply an activation function  $\rho : \mathbb{R} \rightarrow \mathbb{R}$  element-wise. We apply the same fixed activation function across all layers, although each layer theoretically could have a distinct (trainable) activation function. With these definitions, the NN is a parametrisable function  $\mathcal{N}(\boldsymbol{\theta}) : \mathbb{R}^d \rightarrow \mathbb{R}^{n_L}$  defined as

$$\mathcal{N}(\boldsymbol{\theta}) = \Theta_L \circ \rho \circ \Theta_{L-1} \circ \dots \circ \rho \circ \Theta_1, \quad (13)$$

where  $\boldsymbol{\theta}$  represents all the trainable network parameters  $\mathbf{W}_k$  and  $\mathbf{b}_k$ . We denote the network nonlinear manifold space with  $\mathcal{N}$  and a realisation of it with  $\mathcal{N}(\boldsymbol{\theta})$ .

**2.5. Compatible finite element interpolated neural networks.** For simplicity, we focus on the Maxwell's problem (1) in this section. We shall discuss the Darcy problem in Sect. 2.6. Our approach to the neural discretisation relies on finding a NN such that its interpolation into  $U_{h,0}^1$  minimises a discrete dual norm of the residual  $\mathcal{R}_h$  over the test space  $V_{h,0}^1$ .

The compatible FEINN method combines the compatible FE discretisation (9) and the NN (13) by integrating a NN  $\mathbf{u}_N$  into the FE residual (10). This leads to the following non-convex optimisation problem:

$$\mathbf{u}_N \in \arg \min_{\mathbf{w}_N \in \mathcal{N}} \mathcal{L}(\mathbf{w}_N), \quad \mathcal{L}(\mathbf{w}_N) \doteq \left\| \mathcal{R}_h(\pi_{h,0}^1(\mathbf{w}_N)) \right\|_{V_0^1}. \quad (14)$$

Other choices of the residual norm are discussed in Sect. 2.7. We note that some NN architectures are not compact and the minimum cannot be attained but approximated up to any  $\epsilon > 0$  in a meaningful norm. We refer to [18] for more details.

Compatible FEINNs make use of the appropriate interpolators for the functional space in which the problem is posed, determined by the discrete de Rham complex. This approach maintains all the advantages of the FEINNs in [16, 18] for grad-conforming approximations. We stress the fact that the boundary conditions are incorporated in the method by the interpolation operator  $\pi_{h,0}^1$  on the FE space with zero trace and the FE offset  $\bar{\mathbf{u}}_h$ . Unlike PINNs [9, 12], there is no need to incorporate these conditions as penalties in the loss, nor to impose them at the NN level using distance functions as in [14, 15]. Furthermore, since compatible FE bases are polynomials, the integrals in the FE residual can be computed exactly using Gaussian quadrature rules, avoiding issues with Monte Carlo integration [36] and the need for adaptive quadratures [13]. Besides, relying on a discrete FE test space, one can use the dual norm of the residual in the loss function, which is essential in the numerical analysis of the method [18] and has been experimentally observed beneficial in the training process.

**2.6. Trace finite element interpolated neural networks.** Based on the approach to FE discretisation discussed in Sect. 2.3.5, we introduce the trace FEINN method for approximating (4). The optimisation problem involves two NNs  $\mathbf{u}_N$  and  $p_N$ , and reads:

$$\mathbf{u}_N, p_N \in \arg \min_{\mathbf{w}_N, q_N \in \mathcal{N}_u \times \mathcal{N}_p} \mathcal{L}(\mathbf{w}_N, q_N), \quad \mathcal{L}(\mathbf{w}_N, q_N) \doteq \left\| \mathcal{R}_h(\pi_h^2(\mathbf{w}_N), \pi_h^3(q_N)) \right\|_{V_2' \times V_3'}. \quad (15)$$

Note that both NNs are defined in  $\mathbb{R}^3$ . Besides,  $\mathbf{u}_N$  is not necessarily tangent to  $S$ . This method is coined with the term trace FEINNs due to its resemblance to TraceFEM [30] (as it seeks an approximation of the surface PDE on a finite-dimensional manifold living in a higher dimensional space). However, we stress that, as opposed to TraceFEM, it does not need stabilisation terms in the loss function to restrict the problem and unknowns to the tangent space, as it relies on the interpolation onto surface FE spaces defined on  $S_h$ . Additionally, although it would be possible to use a single NN with  $d + 1$  output neurons for both the flux and pressure fields, here we use separate NNs for each field to allow more flexibility in their design, as each solution field may have distinct features.

Since we are considering a closed surface, we do not need to impose boundary conditions on the NN output. For non-empty boundaries, the boundary conditions can be incorporated in the loss function using the interpolant  $\pi_{h,0}^2$ .

**2.7. Loss functions.** The FE residual  $\mathcal{R}_h$  (e.g., the one in (10)) is isomorphic to the vector  $[\mathbf{r}_h(\mathbf{w}_h)]_i = \langle \mathcal{R}_h(\mathbf{w}_h), \varphi^i \rangle \doteq \mathcal{R}_h(\mathbf{w}_h)(\varphi^i)$ , where  $\{\varphi^i\}_{i=1}^N$  are the bases that span  $V_h^i$ , for  $i = 0, \dots, 3$ . Thus, we can use the following loss function:

$$\mathcal{L}(\mathbf{u}_N) = \left\| \mathbf{r}_h(\pi_{h,0}^i(\mathbf{u}_N)) \right\|_{\chi}, \quad (16)$$

where  $\|\cdot\|_{\chi}$  is an algebraic norm. The  $\ell^2$  norm is often used in the PINNs literature [9, 12, 14] and has proven effective in many FEINN experiments [16, 18]. However, the Euclidean norm of  $\mathbf{r}_h$  is a variational crime and this choice is ill-posed in the limit  $h \rightarrow 0$ ; at the continuous level, the  $L^2$ -norm of  $\mathcal{R}(\mathbf{u})$  is not defined in general.

As proposed in [16, 18], we can instead use a *discrete dual norm* in the loss (14) by introducing a discrete Riesz projector  $\mathcal{B}_h^{-1} : V_{h,0}^{i'} \rightarrow V_{h,0}^i$  such that

$$\mathcal{B}_h^{-1} \mathcal{R}_h(\mathbf{w}_h) \in V_{h,0}^i : \left( \mathcal{B}_h^{-1} \mathcal{R}_h(\mathbf{w}_h), \mathbf{v}_h \right)_{U^i} = \mathcal{R}_h(\mathbf{w}_h)(\mathbf{v}_h), \quad \forall \mathbf{v}_h \in V_{h,0}^i,$$

where  $\mathcal{B}_h$  is (approximately) the corresponding Gram matrix in  $V_{h,0}^i$  (the one corresponding to the  $H(\mathbf{curl})$  or  $H(\mathbf{div})$  inner product in this work). The  $\mathcal{B}_h$ -preconditioned loss function can be rewritten as

$$\mathcal{L}(\mathbf{u}_N) = \left\| \mathcal{B}_h^{-1} \mathcal{R}_h(\pi_{h,0}^i(\mathbf{u}_N)) \right\|_{\Upsilon}, \quad (17)$$

The dual norm of the residual in  $V_{h,0}^i$  is attained by using  $\Upsilon = U^i$  (i.e., or  $H(\mathbf{curl}; \Omega)$  or  $H(\mathbf{div}; \Omega)$  norm). This is the case that is needed for obtaining optimal error estimates in [18]. However, other choices, e.g.,  $L^2(\Omega)^d$  are possible. In practice, one can consider any spectrally equivalent approximation of  $\mathcal{B}_h$ , a preconditioner, to reduce computational costs; e.g. the geometric multigrid (GMG) preconditioner is effective for the Poisson equation, as shown in [16]. Effective multigrid solvers for  $H(\mathbf{curl})$  and  $H(\mathbf{div})$  have been designed (see, e.g., [37]), and can be used to reduce the computational cost of the proposed approach.

After interpolation,  $\pi_{h,0}^1(\mathbf{u}_N) \in U_{h,0}^1$  vanishes on  $\Gamma_D$ , ensuring that the FEINN solution  $\pi_{h,0}^1(\mathbf{u}_N) + \bar{\mathbf{u}}_h$  strongly satisfies the Dirichlet boundary conditions. In FEM,  $\bar{\mathbf{u}}_h$  is a standard component and can be computed efficiently. Our method provides a simple and effective way to strongly enforce these conditions, avoiding the need for penalty terms in the loss function [9], or the use of distance functions [14, 15]. Additionally, Gaussian quadrature rules allow efficient and exact computation of the integrals in (17). Spatial derivatives are now calculated using the polynomial FE basis functions, which are more efficient than hybrid automatic differentiation (mixed derivatives with respect to parameters and inputs) widely used in standard PINN methods. Furthermore, the use of a residual dual function (i.e., the inclusion of preconditioners) further ensures well-posedness of the problem and accelerates training convergence.

The formulation can readily be extended to multifield problems. For the Darcy problem above, the loss defined by the residual vector is

$$\mathcal{L}(\mathbf{u}_N, p_N) = \left\| \mathbf{r}_h(\pi_h^2(\mathbf{u}_N), \pi_h^3(p_N)) \right\|_{\chi}. \quad (18)$$

This simple yet effective loss function is adopted in the numerical experiments discussed below. We can also consider the multifield loss function

$$\mathcal{L}(\mathbf{u}_N, p_N) = \left\| \mathcal{B}_h^{-1} \mathcal{R}_h(\pi_h^2(\mathbf{u}_N), \pi_h^3(p_N)) \right\|_{U^2 \times U^3}, \quad (19)$$

where  $\mathcal{B}_h^{-1}$  is the Gram matrix in  $V_h^2 \times V_h^3$ .

**2.8. Extension to inverse problems.** Given, e.g., partial or noisy observations of the states, inverse problem solvers aim to estimate unknown model parameters and complete the state fields. In [16], the use of FEINNs for solving inverse problems has been extensively discussed. We extend the idea to compatible FEINNs in this section. We denote the unknown model parameters as  $\mathbf{\Lambda}$ , which may include physical coefficients, forcing terms, etc. We approximate  $\mathbf{\Lambda}$  with one or several NNs denoted by  $\mathbf{\Lambda}_N$ . For exact integration, we introduce the interpolants  $\pi_h$  to interpolate  $\mathbf{\Lambda}_N$  onto FE spaces.

Let us consider a discrete measurement operator  $\mathcal{D}_h : U_h^i \rightarrow \mathbb{R}^{M \times d}$  and the observations  $\mathbf{d} \in \mathbb{R}^{M \times d}$ , where  $M \in \mathbb{N}$  is the number of measurements. The loss function for the inverse problem reads:

$$\mathcal{L}(\mathbf{\Lambda}_N, \mathbf{u}_N) \doteq \left\| \mathbf{d} - \mathcal{D}_h(\pi_{h,0}^i(\mathbf{u}_N) + \bar{\mathbf{u}}_h) \right\|_{\ell^2} + \alpha \left\| \mathcal{R}_h(\pi_h(\mathbf{\Lambda}_N), \pi_{h,0}^i(\mathbf{u}_N)) \right\|_{\Upsilon}, \quad (20)$$

where  $\alpha \in \mathbb{R}^+$  is a penalty coefficient for the PDE constraint.

**2.9. Numerical analysis.** The analysis of FEINNs has been carried out in [18] in a general setting. The analysis of compatible FEINNs fits the same framework. We summarise below the main results of this analysis. The well-posedness of the continuous problem relies on the inf-sup condition: there exists a constant  $\beta_0 > 0$  such that

$$\inf_{\mathbf{w} \in U} \sup_{\mathbf{v} \in U} \frac{a(\mathbf{w}, \mathbf{v})}{\|\mathbf{w}\|_U \|\mathbf{v}\|_U} \geq \beta_0, \quad (21)$$

where  $U$  is the functional space where the solution of the PDE is sought (we omit the  $i$  superscript in this section). Besides, the bilinear form must be continuous, i.e., there exists a constant  $\gamma > 0$  such that

$$a(\mathbf{u}, \mathbf{v}) \leq \gamma \|\mathbf{u}\|_U \|\mathbf{v}\|_U, \quad \forall \mathbf{u}, \mathbf{v} \in U. \quad (22)$$

Using a Petrov-Galerkin discretisation, the discrete problem is well-posed if a discrete inf-sup condition is satisfied: there exists a constant  $\beta > 0$  independent of the mesh size  $h$  such that

$$\inf_{\mathbf{w}_h \in U_h} \sup_{\mathbf{v}_h \in V_h} \frac{a(\mathbf{w}_h, \mathbf{v}_h)}{\|\mathbf{w}_h\|_U \|\mathbf{v}_h\|_U} \geq \beta, \quad \beta > 0, \quad (23)$$

where  $U_h \subset U$  and  $V_h \subset U$  are the discrete trial and test spaces, respectively. The discrete inf-sup condition, using  $k_U = k_V$ , is satisfied for the compatible FE spaces being used in this work, which is a direct consequence of the cochain projection between the continuous and discrete de Rham complexes. Using other FE spaces, such as Lagrange elements, fails the discrete inf-sup condition, making the discrete problem ill-posed. In such cases, regularisation is required to ensure a well-posed FE problem. See [7, 38, 39] for more details. For the Petrov-Galerkin discretisation with linearised test spaces, i.e.,  $k_U > k_V = 1$ , we are not aware of any results in the literature. However, the experimental evaluation of condition numbers for the spaces being considered in this paper indicate that this inf-sup condition is satisfied for all the orders being considered in this work. Under these conditions, the following *nonlinear Cea's lemma* holds, where we assume that the NN can emulate the FE space for simplicity (see [18] for a more general statement).

**Theorem 2.3.** *For any  $\epsilon > 0$ , the minimum  $\mathbf{u}_N$  of (14) holds the following a priori error estimate:*

$$\|\mathbf{u} - \pi_h(\mathbf{u}_N)\|_U \leq \rho \inf_{\mathbf{w}_h \in \mathcal{N}_h} \|\mathbf{u} - \mathbf{w}_h\|_U. \quad (24)$$

We note that this result is strong because it shows that the minimum of the loss function of the FE residual is quasi-optimal on the NN manifold, thus exploiting the nonlinear power of this approximation. However, the proof only bounds the error of the FE interpolation of the NN solution, not the error of the NN itself, which is experimentally observed to be much lower in most cases (see [18] for a discussion on this topic).

### 3. NUMERICAL EXPERIMENTS

In this section, we conduct two comprehensive sets of numerical experiments for forward and inverse problems involving Maxwell's and Darcy equations, the latter being posed on the sphere. In the forward experiments, we compare the performance of compatible FEINNs against FEM. Our results show that compatible FEINNs achieve higher accuracy than FEM when the solution is smooth. The use of weak residual discrete dual norms (built out of the inverse of a Gram matrix, or an approximation to it, i.e., a preconditioner) further improves the stability and performance of compatible FEINNs. However, the accuracy improvements can hardly overcome the extra cost of the training process compared to FEM. The use of a fixed mesh for the NN interpolation prevents the effective exploitation of NN nonlinear approximation properties. For this reason, we consider in a second stage the use of adaptive FEINNs and inverse problems.

First, we use  $h$ -adaptive FEINNs to attack problems with localised features, demonstrating that the trained NNs outperform FEM solutions for sharp-feature analytic solutions and match FEM accuracy for singular solutions, all without nested loops. In the inverse problem experiments, we focus on recovering the unknown physical parameters of Maxwell's equations from partial or noisy observations, using the training strategy proposed in [16]. We compare the performance of compatible FEINNs with the adjoint NN method. With partial observations, the addition of an extra NN in the compatible FEINN method improves the accuracy of both the predicted parameters and recovered states compared to the adjoint NN method. When the observations are noisy, compatible FEINNs achieve comparable performance to the adjoint NN method *without any regularisation terms in the loss function*.

We omit the comparison of the FEINN method with other NN-based approaches, such as PINNs and VPINNs. This comparison is already studied in detail in [14, 16]. These studies find that the interpolated NN approach performs similar to or better than PINNs or VPINNs for a given number of NN evaluations. Additionally, the computational cost of interpolated NNs is lower than that of standard PINN methods, as spatial derivatives of NNs are handled using polynomial interpolation. Furthermore, as demonstrated in [16, 18], FEINN convergence can be significantly improved by using preconditioned losses.

**3.1. Implementation.** The implementation details of FEINNs for forward and inverse problems with weak solutions in  $H^1$  are provided in [16], and those for  $h$ -adaptive FEINNs are included in [18]. In this section, we briefly discuss the additional features required for compatible and trace FEINNs, specifically the interpolation of NNs onto Nédélec or RT FE spaces.

We implement the compatible FEINNs method using the Julia programming language. The compatible FEM part is handled by the `Gridap.jl` [40, 41] package, and the NN part is implemented using the `Flux.jl` [42] package. Loss function gradient propagation is managed through user-defined rules with the `ChainRules.jl` [43] package. For adaptive FEINNs, we rely on the `GridapP4est.jl` [44] package to handle forest-of-octrees meshes.

The implementation of NN interpolations onto Nédélec or RT FE spaces is as follows. For each moment-based DoF (e.g., the integral of the normal component of the network over a  $S_h$  cell edge for lowest-order RT FEs on the discrete manifold), we evaluate the NN at the quadrature points and multiply the results by the corresponding weights to compute the DoF value. Since, for a fixed mesh, the quadrature points and weights are fixed for each DoF, they can be extracted and stored once, and reused thereafter at each training iteration. For non-conforming FE spaces, we only need to interpolate NNs onto the master DoFs and use multi-point constraints to compute the slave DoFs values [32, 45].

**3.2. Forward problems.** To evaluate the accuracy of the identified solutions  $p^{id}$  and  $\mathbf{u}^{id}$  for forward problems, we compute their  $L^2$  and  $H(\mathbf{curl})$  or  $H(\mathbf{div})$  error norms:

$$\begin{aligned} e_{L^2(\Omega)}(p^{id}) &= \|p - p^{id}\|_{L^2(\Omega)}, & e_{L^2(\Omega)^d}(\mathbf{u}^{id}) &= \|\mathbf{u} - \mathbf{u}^{id}\|_{L^2(\Omega)^d}, \\ e_{H(\mathbf{curl};\Omega)}(\mathbf{u}^{id}) &= \|\mathbf{u} - \mathbf{u}^{id}\|_{H(\mathbf{curl};\Omega)}, & e_{H(\mathbf{div};\Omega)}(\mathbf{u}^{id}) &= \|\mathbf{u} - \mathbf{u}^{id}\|_{H(\mathbf{div};\Omega)} \end{aligned}$$

where  $p : \Omega \rightarrow \mathbb{R}$  and  $\mathbf{u} : \Omega \rightarrow \mathbb{R}^d$  are the true states. We use sufficient Gauss quadrature points for the integral evaluation to guarantee the accuracy of the computed errors. To simplify the notation, if there is no ambiguity, we omit the domain  $\Omega$  and dimension  $d$  in the following discussions.

In all forward problem experiments, we use the same NN architecture as in [16], i.e., 5 hidden layers with 50 neurons each, and `tanh` as activation function. Unless otherwise specified, the default training losses are (16) and (18) with the  $\chi = \ell^2$  norm. We explicitly state when preconditioned losses (17) and (19) are used, along with the type of preconditioners and dual norms. Besides, the test FE spaces we employ are always linearised, i.e., lowest-order FE basis built upon refinement of the trial FE mesh if the order of the trial space is not the lowest possible.

In addition to measuring the performance of the interpolated NNs, we are also interested in how well the NNs satisfy the Dirichlet boundary condition. We note that Dirichlet boundary condition is implicitly enforced to the NN via the FE residual minimisation. After the training process, in which the interpolated NN is used to compute the loss and gradients, we obtain a NN solution  $\mathbf{u}_N$ . With this solution, we can evaluate the error of the interpolated NN, i.e.,  $\pi_{h,0}(\mathbf{u}_N) + \bar{\mathbf{u}}_h - \mathbf{u}$ , or the NN itself, i.e.,  $\mathbf{u}_N - \mathbf{u}$ , where  $\mathbf{u}$  is the true solution. In each plot within this section, the label ‘‘FEINN’’ denotes results for the interpolation of the NN solutions, while the label ‘‘NN’’ indicates results for the NNs themselves (using very accurate quadratures to approximate integrals of NNs). For reference, we display the FEM solution using Petrov-Galerkin discretisation in the plots, labelled as ‘‘FEM’’.

For all the forward and inverse problem experiments, we use the Glorot uniform method [46] to initialise NN parameters and the BFGS optimiser in `Optim.jl` [47] to train the NNs.

**3.2.1. Maxwell’s equation with a smooth solution.** For the first set of experiments, we consider the forward Maxwell problem with a smooth solution. We adopt most of the experimental settings from [32, Sect. 6.1], where the domain is the unit square  $\Omega = [0, 1]^2$  with a pure Dirichlet boundary ( $\Gamma_D = \partial\Omega$ ). We pick  $\mathbf{f}$  and  $\mathbf{g}$  such that the true state is:

$$\mathbf{u}(x, y) = \begin{bmatrix} \cos(4.6x) \cos(3.4y) \\ \sin(3.2x) \sin(4.8y) \end{bmatrix}.$$

We first fix the order of the trial basis functions, i.e.,  $k_U$  is fixed, and refine the mesh to study the convergence of the errors. Considering that the initialisation of NN parameters may affect the results, at each mesh resolution, we repeat the experiment 10 times with different NN initialisations. The results are shown in Fig. 1. The dashed lines in the plots represent FEM errors. Different markers distinguish the results of NNs and their interpolations, and different colours indicate results for different  $k_U$ . FEM results exhibit the expected Galerkin’s FEM theoretical error convergence rate of  $O(h^{k_U})$  measured both in  $L^2$  and  $H(\mathbf{curl})$  norms.

Since the variance for FEINN results with the same mesh size and  $k_U$  is negligible, we display the mean values of these 10 runs. We observe that both the  $L^2$  and  $H(\mathbf{curl})$  errors of FEINNs consistently fall on the corresponding FEM lines for both  $k_U = 1$  and  $k_U = 2$ , indicating successful training and accurate FEINN

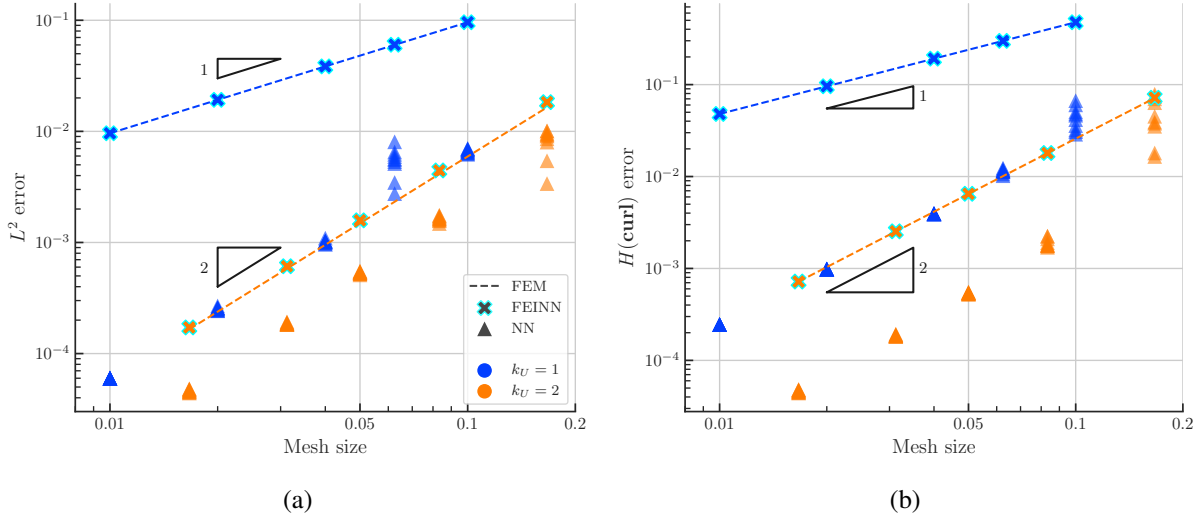


FIGURE 1. Error convergence of FEINN and NN solutions with respect to the mesh size of the trial FE space for the forward Maxwell problem with a smooth solution. Different colours represent different orders of trial bases.

solutions. For the NNs, the errors are always below the corresponding FEM lines, suggesting that the NNs not only accurately satisfies the Dirichlet boundary condition but also provide more accurate results than the FEM solutions. For example, in Fig. 1a, with  $h = 0.01$  and  $k_U = 1$ , the NN is more than 2 orders of magnitude more accurate than the FEM solution. Similar observations are found for the  $H(\text{curl})$  error in Fig. 1b. These findings extend the conclusion in [16] that NNs can outperform FEM solutions for the Poisson equation with smooth solutions to the Maxwell’s equations. For  $k_U = 2$ , the difference between the NN and the FEM results is less pronounced than for  $k_U = 1$ , but NNs still beat the FEM solutions. Besides, with a fine enough mesh, and  $k_U = 1$ , it is remarkable to find that the convergence rate of the NNs matches the  $k_U = 2$  FEM rate. This suggests that NNs can bring superconvergence in certain scenarios. The improved accuracy of the NNs compared to the FEM solutions is likely attributed to the smoothness of the NN solutions: the  $C^\infty$  NN solution (with the  $\tanh$  activation function) outperforms the  $C^0$  FEM solution when approximating a smooth true state.

3.2.2. *The effects of preconditioning on Maxwell’s equation.* It is well-known that the condition number of the matrix arising from the FE discretisation of Maxwell’s problem grows with  $k_U^2$  and  $h^{-2}$ . From preliminary experiments, we observe that NN training becomes more difficult as  $k_U$  increases, which is somehow expected by the condition number bounds, resulting in a more challenging optimisation problem. In this experiment, we explore the possibility of using the dual norm of the residual, i.e., the preconditioned loss (17), to reduce the optimisation difficulty and improve training efficiency and accuracy. We consider the same problem as in Sect. 3.2.1, with  $h = 2^{-4}$  and  $k_U = 4$ . We employ the  $\mathbf{B}_{\text{in}}$  preconditioner, defined as the Gram matrix of the  $H(\text{curl})$  inner product on the linearised FE space (used as both trial and test spaces). Alternative preconditioners, e.g., the GMG preconditioner for Maxwell’s equations [48], could also be considered.

In Fig. 2, we juxtapose the  $H(\text{curl})$  error histories of NNs and their interpolations during training at the second step, using the dual norm (with preconditioning) and the Euclidean norm (without preconditioning) of the residual vector. To further improve training efficiency, we explore a two-step training strategy, in which we compute the FE solution at the interpolation quadrature points as training data, and initialise the NNs by performing a data fitting task with this data. Next, we train the NNs with the preconditioned PDE loss (17). Note that the first step is computationally much cheaper than the second. An initialisation step with 4,000 iterations is applied to the NNs before the PDE training. As a reference, we also display the results without initialisation and preconditioning (labelled as “0k + N/A” in the figure). We use the  $H(\text{curl})$  (dual) norm and the  $L^2$  norm of the Riesz representative of the residual in the preconditioned loss (17).

The initialisation step significantly accelerates the convergence of the training process, as indicated by the lower initial errors in Fig. 2. Besides, we observe that unpreconditioned NN errors spike at the

beginning, while preconditioned NNs maintains a stable error reduction throughout the entire second step. This demonstrates that the well-defined preconditioned loss provides more stable training compared to the residual vector based loss.

More interestingly, as shown in Fig. 2b, with the  $H(\mathbf{curl})$  norm, the NN solution starts outperforming the FEMs solution after around 1,500 iterations and achieves nearly an order of magnitude lower  $H(\mathbf{curl})$  error by 6,000 iterations. The preconditioned PDE training serves as a post-processing step to improve FE solution accuracy (more than one order of magnitude in the experiments) without increasing the mesh resolution or trial order. In summary, the initialisation step, while not required, can lower computational cost and provide faster error reduction. Moreover, the  $\mathbf{B}_{\text{lin}}$  preconditioner, combined with  $L^2$  or  $H(\mathbf{curl})$  norms in the loss (17), greatly accelerates NN convergence and improves the accuracy of the trained NNs. These results suggest that these schemes can be effective for transient problems, where the NN will be properly initialised with the solution at the previous time step.

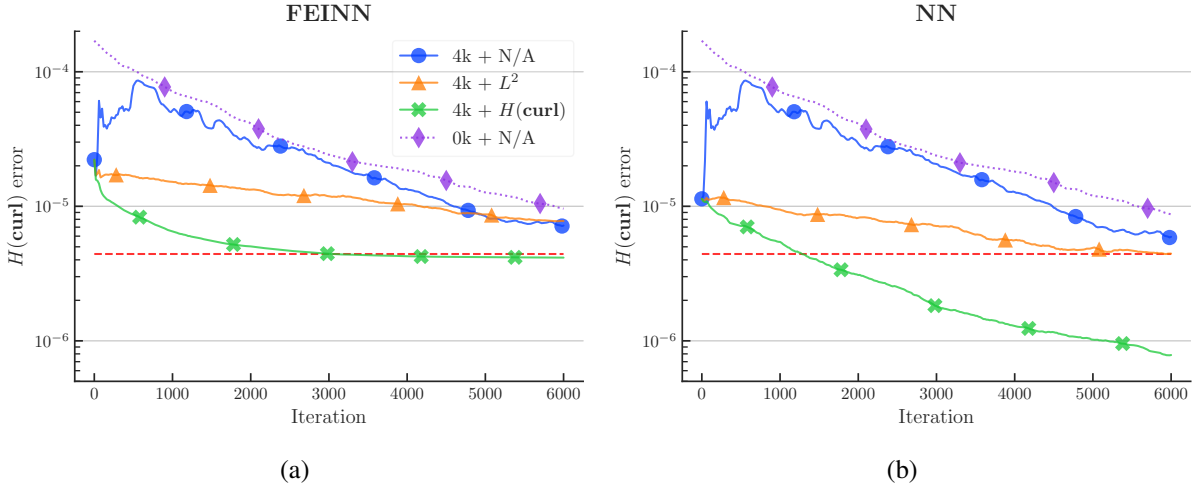


FIGURE 2.  $H(\mathbf{curl})$  error history of and FEINNs and NNs during training using different dual norms in the preconditioned loss for the forward Maxwell problem with a smooth solution; “N/A” indicates no preconditioning. The number in the legends indicates iterations in the initialisation step. Mesh size  $h = 2^{-4}$  and order  $k_U = 4$  were used.

With  $\mathbf{u} \in C^\infty(\bar{\Omega})$  and an effective preconditioner, we can now investigate how the error behaves with increasing  $k_U$ . We revisit the same problem as in Sect. 3.2.1, keeping the mesh size  $h$  fixed and increasing  $k_U$  from 1 to 4. The errors versus  $k_U$  are presented in Fig. 3. For each order, we also run 10 experiments, and only the mean values of the FEINN errors are displayed. We employ the preconditioner  $\mathbf{B}_{\text{lin}}$  equipped with  $H(\mathbf{curl})$  dual norm during training. We investigate two mesh sizes,  $h = 1/15$  and  $h = 1/30$ , distinguished by different colours in the figure. We observe that, similar to the findings reported in [16], the FEINN errors can still recover the corresponding FEM errors as  $k_U$  increases, and the NN errors are always below the FEM errors. For instance, when  $k_U = 3$  and  $h = 1/30$ , the NN solutions outperform the FEM solution by more than one order of magnitude in both  $L^2$  and  $H(\mathbf{curl})$  errors. Besides, preconditioners also enhance the accuracy of NN solutions. For  $k_U = 2$  and  $H(\mathbf{curl})$  errors, the preconditioned NN solutions, as shown in Fig. 3b, surpass the FEM solution by two orders of magnitude. In contrast, without preconditioning, depicted in Fig. 1b, the NN solutions exceed the FEM solutions by only one order of magnitude. It is noteworthy to mention that, as  $k_U$  increases, the NN errors approach the FEM errors, suggesting a potential need for enrichments in the NN architecture. However, studying the effects of different NN architectures is beyond the scope of this paper.

3.2.3. *Darcy equation on a sphere.* We now attack a Darcy problem defined on the unit sphere  $S = \{(x, y, z) : x^2 + y^2 + z^2 = 1\}$ . We refer to Sect. 2.6 for the trace FEINN approach to solve this problem. We adopt the following analytical solutions from [35, Sect. 5.1.1]:

$$\mathbf{u}(x, y, z) = \frac{1}{x^2 + y^2 + z^2} \begin{bmatrix} y^3z - 2x^2yz + yz^3 \\ x^3z - 2xy^2z + xz^3 \\ x^3y - 2xyz^2 + xy^3 \end{bmatrix}, \quad p(x, y, z) = -xyz.$$

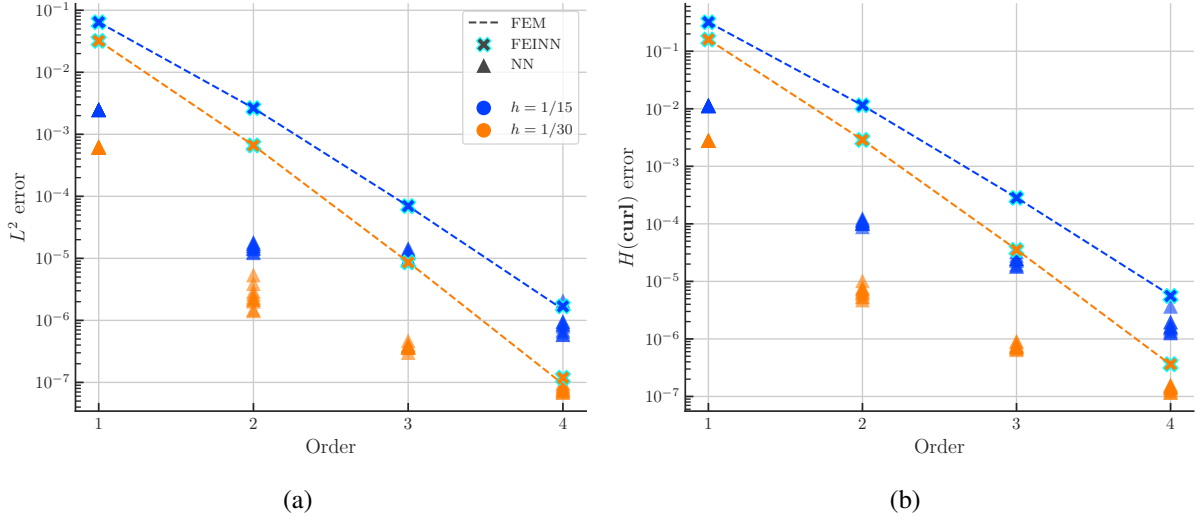


FIGURE 3. Error convergence of FEINN and NN solutions with respect to the order of trial bases for the forward Maxwell problem with a smooth solution. Loss function subject to minimisation is equipped with preconditioner  $\mathbf{B}_{\text{lin}}$  and the  $H(\text{curl})$  norm. Different colours represent different mesh sizes.

The source term is  $f(x, y, z) = -12xyz$ . Note that the analytical  $p$  satisfies the zero mean property on  $S$ , i.e.,  $\int_S p = 0$ .

Since the problem has no boundary conditions, given a solution  $(\mathbf{u}, p)$ , another valid solution can be obtained by adding an arbitrary constant to  $p$ . To ensure solution uniqueness, we use a (scalar) Lagrange multiplier to impose the global zero mean constraint. This approach is widely used in the FEM community and it ensures that the discretisation matrix is invertible, making the FE problem well-posed. We then revise the weak formulation in (5) as follows: find  $(\mathbf{u}, p, \lambda) \in U^2 \times \tilde{U}^3 \times \mathbb{R}$  such that

$$(\mathbf{u}, \mathbf{v}) - (p, \nabla_S \cdot \mathbf{v}) = 0 \quad \forall \mathbf{v} \in U^2, \quad (\nabla_S \cdot \mathbf{u}, q) + (\lambda, q) = (f, q) \quad \forall q \in \tilde{U}^3, \quad (p, \sigma) = 0 \quad \forall \sigma \in \mathbb{R}.$$

The corresponding FE formulation is similar to (11).

To discretise the domain, we employ the so-called cubed sphere [34]. This mesh is available in the `GridapGeosciences.jl` [49] package, a `Gridap.jl`'s extension for the numerical approximation of geophysical flows [50]. In the experiments, each of the six panels of the cubed sphere is discretised with  $n_e \times n_e$  quadrilateral elements, where  $n_e$  is the number of elements on each side of the panel. Thus, the total number of elements is  $6 \times n_e \times n_e$ .

As mentioned in Sect. 2.6, we use two NNs  $\mathbf{u}_N$  and  $p_N$  to represent the flux and the pressure, respectively. We use first-order RT spaces to interpolate  $\mathbf{u}_N$  and piecewise-constant discontinuous Galerkin (DG) spaces to interpolate  $p_N$ . The NN interpolation onto DG spaces is the same as that onto continuous Galerkin (CG) spaces covered in [16, 18], which is just defined at the evaluation of  $p_N$  at the nodes of the FE space.

Fig. 4 shows the interpolated NN solutions for the flux, its divergence, and the pressure on a cubed sphere mesh consisting of  $6 \times 50 \times 50$  quadrilateral elements. Note that the flux solution in Fig. 4a is tangential to the sphere by construction of the RT space. In Fig. 4b, the flux divergence displays discontinuities at element boundaries because RT bases have  $C^0$  continuous normal components. Fig. 4c demonstrates that the pressure solution exhibits a form of symmetry, likely leading to a zero mean on the sphere.

Next, we analyse the convergence of the trace FEINN method with respect to mesh size ( $h \approx 2/n_e$ ). The errors of the interpolated NNs are plotted in Fig. 5. Again, each marker for FEINNs represents the mean value from 10 independent experiments. It is noteworthy to mention that, the flux NN solution is not constrained to be tangential to the sphere. However, its interpolation onto the surface FE space (using RT elements and Piola maps) belongs to the tangent bundle. By interpolating the trained NNs onto a FE space with higher-order bases and a finer mesh, we observed that one can achieve more accurate solutions, *even if a coarser mesh and order were used for training*. A similar phenomenon occurs in data science, such as image super-resolution [51], where NNs trained on lower-resolution images can generate higher-resolution outputs. Specifically, we interpolate the trained flux NNs onto a FE space of order 4 and a

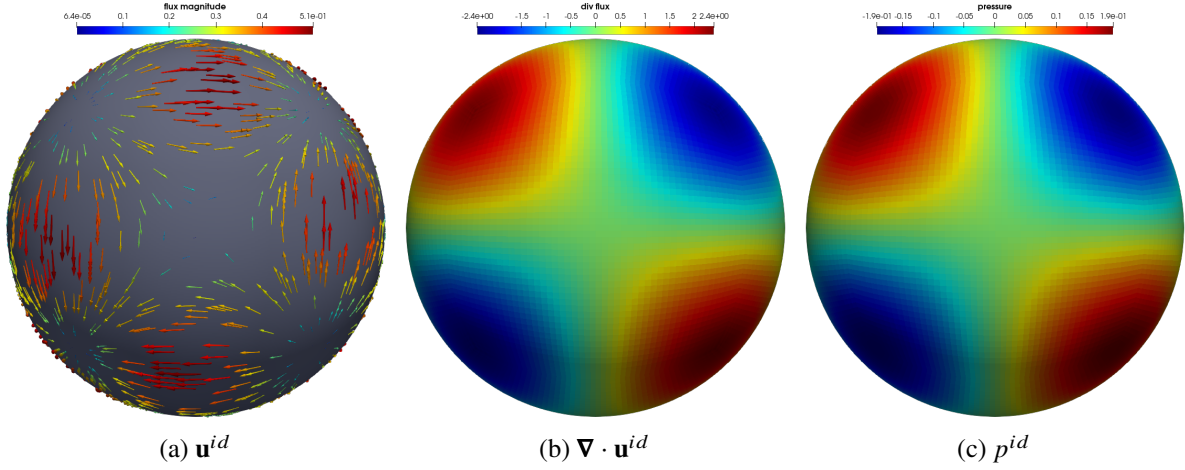


FIGURE 4. Interpolated NN solutions on a  $6 \times 50 \times 50$  grid for the forward Darcy problem on a sphere.

mesh of  $6 \times 200 \times 200$  quadrilateral elements. For convenience, in Fig. 5 and the rest of the section, we refer to both the trained pressure NNs and the interpolations of the trained flux NNs onto a finer mesh as NN solutions, labelled as “NN\*”.

For the interpolated NNs, Fig. 5 shows that they successfully match the FEM solutions for both flux and pressure across various mesh resolutions, with all the FEINN markers aligning on their corresponding FEM lines. Besides, the NN solutions are more accurate than the FEM solutions, especially for the flux: both  $L^2$  and  $H(\text{div})$  errors are more than two orders of magnitude lower than corresponding FEM errors. Besides, a visual comparison of the slopes in Fig. 5a and Fig. 5b indicates that NN solutions exhibit a higher convergence rate than FEM solutions. These findings highlight the potential of NNs in solving surface PDEs more efficiently by training on a coarse mesh and then interpolating onto a fine mesh for the final solution.

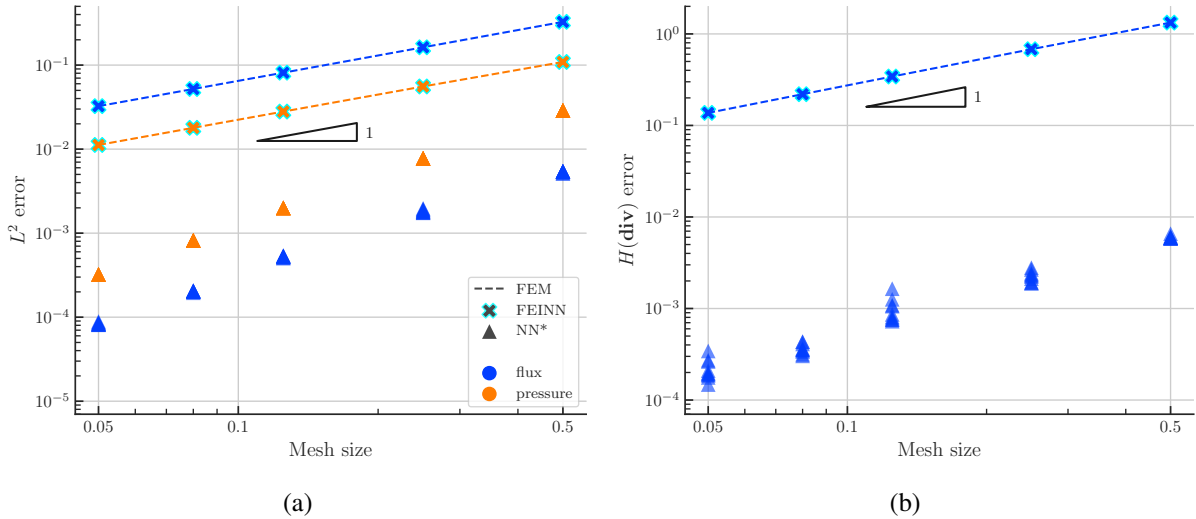


FIGURE 5. Error convergence of FEINN and NN solutions with respect to the mesh size of the trial FE space for the forward Darcy problem on the unit sphere. Colours distinguish between flux and pressure.

**3.2.4. Adaptive training for Maxwell’s equation with localised features.** We conclude the forward experiments section by employing the  $h$ -adaptive FEINN method proposed in [18] to tackle forward Maxwell problems with localised features. We consider both sharp features and singularities in the solution. We first focus on the following analytic solution defined in the unit square domain  $\Omega = [0, 1]^2$  with a pure Dirichlet

boundary:

$$\mathbf{u}(x, y) = \begin{bmatrix} \arctan(50(\sqrt{(x+0.05)^2 + (y+0.05)^2} - 1.2)) \\ 1.5 \exp(-500((x-0.5)^2 + (y-0.5)^2)) \end{bmatrix}.$$

Note that the x-component of  $\mathbf{u}$  has a circular wave front centred at  $(-0.05, -0.05)$  with a radius of 1.2, while the y-component features a sharp peak at  $(0.5, 0.5)$ . These sharp features are typically benchmarks for evaluating the performance of numerical methods equipped with adaptive mesh refinement.

We adopt the train, estimate, mark, and refine strategy proposed in [18] to adaptively refine the mesh and train FEINNs. Preconditioning is applied in the loss function to improve the training stability and to speed up the convergence. We use the  $L^2$  norm in the preconditioned loss function (17) and, similar to [18] and the previous experiment, we utilise the preconditioner  $\mathbf{B}_{\text{lin}}$ . We use different error indicators to guide mesh adaptation. Namely, the  $L^2$  error among the interpolated NN and the analytical solution, the  $L^2$  norm of the difference between the NN and its FE interpolation, and the  $L^2$  norm of the strong PDEs residual evaluated at the NN. These are labelled as “real”, “integration”, and “network”, respectively, in the figures below. We leverage forest-of-octrees meshes for adaptivity, which are typically non-conforming. To maintain curl-conforming property in the FE space, we incorporate additional linear multi-point constraints for slave DoFs. For a more detailed discussion on  $h$ -adaptive FEINN, we refer to [18].

In the experiments, we fix  $k_U = 2$ , with the initial trial FE space consisting of  $16 \times 16$  quadrilateral elements. We refine the mesh up to 7 times, each with a 10% refinement ratio (i.e., we refine 10% of the cells with the largest error indicator), and run 20 independent experiments initialised with different NN parameters for each error indicator. The training iterations for each step are [100, 100, 200, 200, 300, 300, 400, 400], totalling 2000 iterations.

In Fig. 6, we present the convergence of the NN errors with respect to the refinement step. Fig. 6a shows errors measured in the  $L^2$  norm, while Fig. 6b in the  $H(\text{curl})$  norm. The solid line represents the median of the errors, while the band represents the range from the minimum to the 90th percentile across 20 independent runs. The red dashed line illustrates the error of the  $h$ -adaptive FEM solution, using the real FEM  $H(\text{curl})$  error as the refinement indicator.

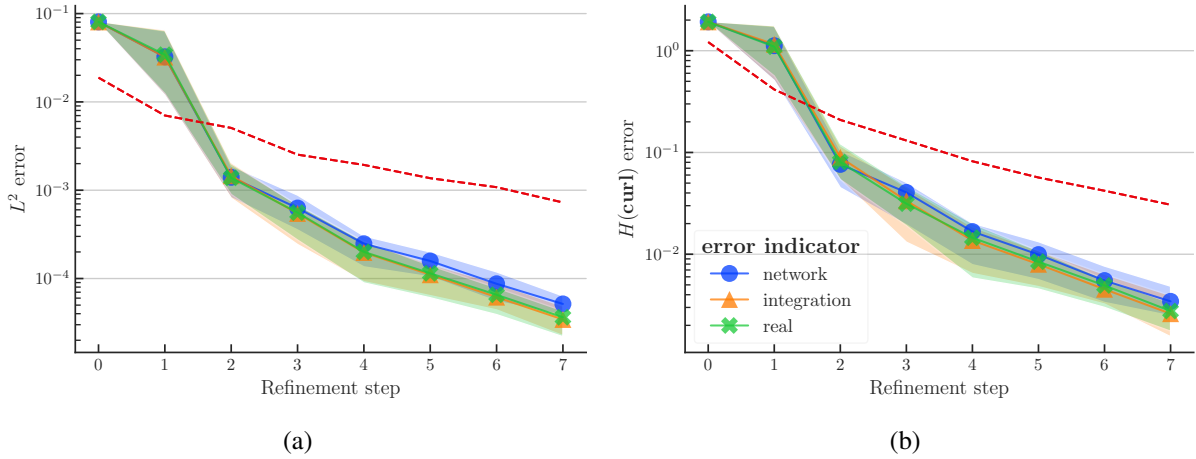


FIGURE 6. Error convergence of NN solutions with respect to refinement steps for the forward Maxwell problem with less smooth solution, using different error indicators. The solid line denotes the median, and the band represents the range from the minimum to the 90th percentile across 20 independent runs. The red dashed line illustrates the  $h$ -adaptive FEM solution error using the real FEM  $H(\text{curl})$  error as the refinement indicator.

Although the trained NNs start with higher errors, they begin to outperform the  $h$ -adaptive FEM solution after the first two refinement steps. As shown in both Fig. 6a and Fig. 6b, the NN errors consistently fall below the FEM error lines after the second refinement. This observation agrees with the findings in [18], where NNs can beat  $h$ -adaptive FEM for smooth analytic solutions. However, in [18], NN solutions are noted to be superior mainly in  $H^1$ -error for Poisson equations, but our Maxwell experiments show lower errors in both  $L^2$  and  $H(\text{curl})$  norms. Furthermore, the network and integration error indicators effectively

guides mesh refinements, as reflected by the closely aligned convergence curves across different indicators. A similar finding was also reported in [18] for the Poisson problems.

Next, we increase the difficulty of the problem by introducing singular feature in the solution. The analytic solution is now defined in the domain  $\Omega = [0, 1]^2$  as follows:

$$\mathbf{u}(x, y) = \nabla\left(r^{\frac{2}{3}} \sin\left(\frac{2\theta}{3}\right)\right), \quad r = \sqrt{x^2 + y^2}, \quad \theta = \arctan\left(\frac{y}{x}\right).$$

This solution exhibits a singularity at the origin and serves as a popular benchmark for testing adaptive methods (see, e.g., [32]). Most of the settings remain the same as the previous experiment, except for the following adjustments: the initial mesh comprises  $20 \times 20$  quadrilateral elements, the  $H(\mathbf{curl})$  norm is used in the preconditioned loss function, and the training iterations are in total 5,000 with [500, 750, 1000, 1250, 1500] iterations for each step.

Fig. 7 displays the convergence of the NN errors across refinement step from 20 independent runs. The NN errors are computed by interpolating the trained NNs onto a second-order FE space on a finer uniform mesh. Despite the low regularity, the NN solutions consistently match the adaptive FEM solutions at each refinement step for both  $L^2$  and  $H(\mathbf{curl})$  errors. The figure also highlights that the proposed network and integration error indicators effectively guide mesh refinements for this singular problem, achieving performance comparable to the real error that is barely available in practice. Overall, Fig. 6 and Fig. 7 illustrate the effectiveness of the  $h$ -adaptive FEINN method in solving  $H(\mathbf{curl})$  problems with sharp features and singularities.

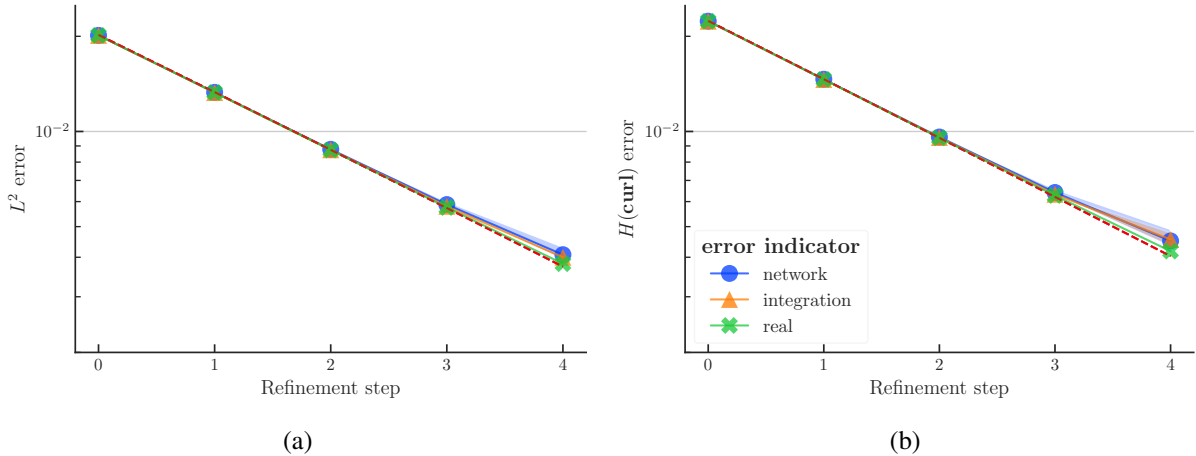


FIGURE 7. Error convergence of NN solutions with respect to refinement steps for the forward Maxwell problem with singularity, using different error indicators. See the caption of Fig. 6 for details about the information displayed in this figure.

**3.3. Inverse problems.** In this section, we present the results of the inverse Maxwell problems, focusing on situations with partial or noisy observations of the state  $\mathbf{u}$  and a fully-unknown coefficient  $\kappa$ . We compare the performance of compatible FEINNs with adjoint NNs for both types of observations. The adjoint NN method was first proposed in [52], and then further explored in [53]. This method approximates the unknown coefficient with a NN and uses the adjoint method to compute the gradient of the data misfit with respect to the NN parameters. While previous works [16, 52, 53] mainly focus on inverse Poisson problems, in this work we extend the comparison to inverse Maxwell’s problems.

For the compatible FEINN method, we employ two NNs,  $\mathbf{u}_N$  and  $\kappa_N$ , to approximate the state and coefficient, respectively. The adjoint NN method only requires a single NN,  $\kappa_N$ , to represent the unknown coefficient. To ensure a fair comparison, we use the same NN architecture for  $\kappa_N$  in both methods. In the plots, the label “AdjointNN” denotes results from the adjoint NN method; the label “FEINN” indicates interpolated NN results from the compatible FEINN method. The label tag “NN only” for FEINNs represents results associated with NNs themselves. Consistent with [16], we use the `softplus` activation function, and apply a rectification function  $r(x) = |x| + 0.01$  as the activation for the output layer of  $\kappa_N$  to ensure its positivity.

We adopt the three-step training strategy proposed in [16] for solving inverse problems with FEINNs. First, we initialise  $\mathbf{u}_N$  by training it with the observations. Then, we fix  $\mathbf{u}_N$  and train  $\kappa_N$  using only the PDE loss. Finally, we fine-tune both  $\mathbf{u}_N$  and  $\kappa_N$  with the full loss (20). The final step contains multiple substeps with increasing penalty coefficients for the PDE term in the loss. We adhere to the convention used in [16] to denote the training iterations and penalty coefficients. For example, [100, 50, 3 × 400] iterations means that the first step involves 100 iterations, the second step has 50 iterations, and the third step comprises three substeps, each with 400 iterations. Similarly,  $\alpha = [0.1, 0.2, 0.3]$  denotes that the penalty coefficients for those substeps are 0.1, 0.2, and 0.3, respectively.

We use the following three relative errors to evaluate the accuracy of the identified state  $\mathbf{u}^{id}$  and coefficient  $\kappa^{id}$ :

$$\varepsilon_{L^2(\Omega)^d}(\mathbf{u}^{id}) = \frac{\|\mathbf{u}^{id} - \mathbf{u}\|_{L^2(\Omega)^d}}{\|\mathbf{u}\|_{L^2(\Omega)^d}}, \quad \varepsilon_{H(\mathbf{curl};\Omega)}(\mathbf{u}^{id}) = \frac{\|\mathbf{u}^{id} - \mathbf{u}\|_{H(\mathbf{curl};\Omega)}}{\|\mathbf{u}\|_{H(\mathbf{curl};\Omega)}}, \quad \varepsilon_{L^2(\Omega)}(\kappa^{id}) = \frac{\|\kappa^{id} - \kappa\|_{L^2(\Omega)}}{\|\kappa\|_{L^2(\Omega)}},$$

where  $\mathbf{u} : \Omega \rightarrow \mathbb{R}^d$  and  $\kappa : \Omega \rightarrow \mathbb{R}^+$  are the true coefficient and state, respectively.

**3.3.1. Partial observations.** In this section, we tackle an inverse Maxwell problem with partial observations of the state. The problem is defined on the unit square  $\Omega = [0, 1]^2$ , with pure Dirichlet boundary conditions. We assume that only the  $x$ -component of the magnetic field  $\mathbf{u}$  is observed, with a total of  $70^2$  observations distributed uniformly within the region  $[0.005, 0.995]^2$ . This region selection avoids observations on the Dirichlet boundary, as the state is fully known there. In addition, one-component observations of a vector-valued field are common in practice [54]. Note that with too few observations, the problem becomes highly ill-posed, leading to identified solutions that diverge significantly from the true ones for both methods. The analytical state  $\mathbf{u}$  (Fig. 8a) and coefficient  $\kappa$  (Fig. 8d) are defined as follows:

$$\mathbf{u}(x, y) = \begin{bmatrix} \cos(\pi x) \cos(\pi y) \\ \sin(\pi x) \sin(\pi y) \end{bmatrix}, \quad \kappa(x, y) = 1 + 5e^{-5((2x-1)^2 + (y-0.5)^2)}.$$

The domain is discretised by  $50 \times 50$  quadrilateral elements. We employ first-order Nédélec elements for  $\mathbf{u}_N$  interpolation, and first-order CG elements for  $\kappa_N$  interpolation. The NN structures are almost identical: both have 2 hidden layers with 20 neurons each, but the output layer of  $\mathbf{u}_N$  has 2 neurons, while the output layer of  $\kappa_N$  has 1 neuron activated by the rectification function  $r(x)$ . For compatible FEINNs, the training iterations for the three steps are [150, 50, 3 × 600], totalling 2,000 iterations, and the penalty coefficients are  $\alpha = [0.001, 0.003, 0.009]$ . The total training iterations for the adjoint NN method is also 2,000.

In the second column of Fig. 8, we present the FEINN solutions for the state and coefficient, and their corresponding errors are displayed in the third column. The state error (see Fig. 8c) is reasonably small compared to the true state (see Fig. 8a), and the identified coefficient (see Fig. 8e) is visually very close to the true coefficient (Fig. 8d).

In Fig. 9, we compare the relative errors between compatible FEINN and adjoint NN solutions. Note that the  $\varepsilon_{L^2}(\kappa^{id})$  for both methods starts with the same value, as the initialisations for  $\kappa_N$  are identical. Compatible FEINNs converge faster than adjoint NNs as all three FEINN error curves fall below the corresponding adjoint NN error curves after 400 iterations. On the downside, the convergence of compatible FEINNs is not as stable as that of adjoint NNs, as the errors for the former fluctuate during training. This raises concerns about whether the superior performance of compatible FEINNs over adjoint NNs is due to a specific NN initialisation. We investigate this in the following experiments.

We repeat the experiment 100 times with different NN initialisations for both FEINNs and adjoint NNs. The resulting box plots for the relative errors are presented in Fig. 10, where whiskers represent the minimum and maximum values within 1.5 times the interquartile range. In this scenario with partial observations, the FEINN method demonstrates greater stability and accuracy compared to the adjoint NN method. The FEINN boxes for all three relative errors are more tightly clustered and positioned lower than the adjoint NN boxes. Looking at the NNs themselves resulting from the FEINNs method, the state NNs are more accurate but less stable compared to their interpolation counterparts. This is evident from Fig. 10, where the NN error boxes are lower but more scattered than the interpolated NN error boxes. In line with the findings in [16], without interpolation, the NN coefficient errors are roughly the same as their interpolation counterparts. Overall, the FEINN method exhibit higher reliability than the adjoint NN method for solving the inverse Maxwell problem with partial observations.

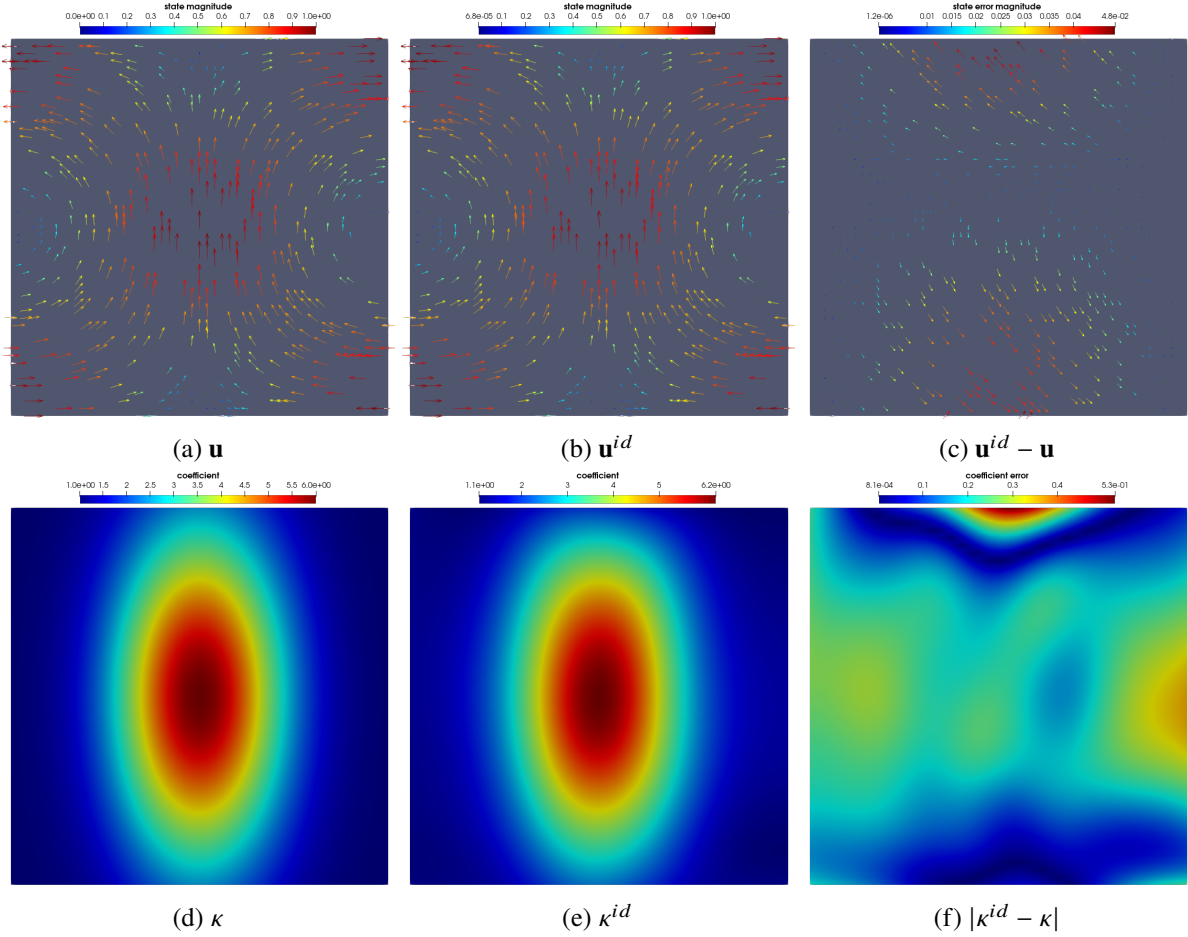


FIGURE 8. Illustration of known analytical solutions (first column), compatible FEINN solutions (second column), and corresponding point-wise errors (third column) for the inverse Maxwell problem with partial observations. Results correspond to an experiment with a specific NN initialisation. The first row depicts the state, while the second row represents the coefficient.

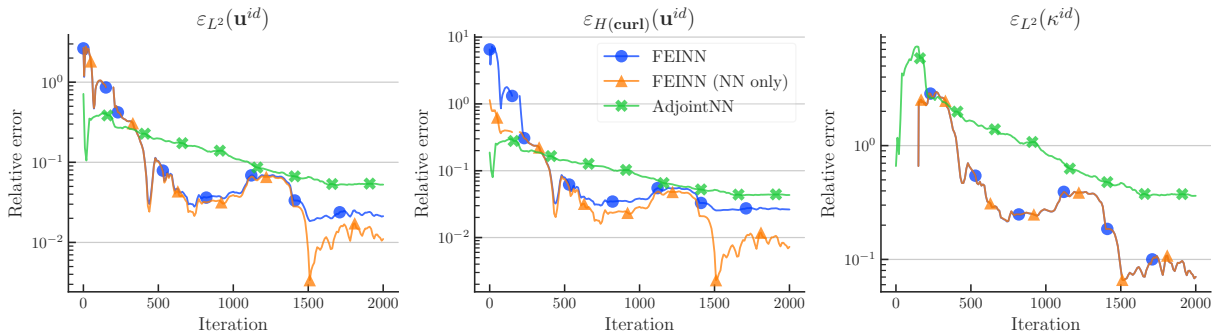


FIGURE 9. Comparison among FEINNs and adjoint NNs in terms of relative errors during training for the inverse Maxwell problem with partial observations. Both optimisation loops were run for 2,000 iterations.

3.3.2. *Noisy observations.* We consider next an alternative inverse Maxwell problem that now involves noisy observations of the state  $\mathbf{u}$ . Unlike the previous experiment, we have access to both components of the data, but they are contaminated with Gaussian noise  $\epsilon \sim N(0, 0.05^2)$ . Note that each observation is computed by adding Gaussian noise to the true state, i.e.,  $\mathbf{u}^{\text{obs}} = (1 + \epsilon)\mathbf{u}$ . We generate  $30^2$  noisy observations distributed uniformly in  $[0.005, 0.995]^2$ . The domain, boundary conditions, and analytical

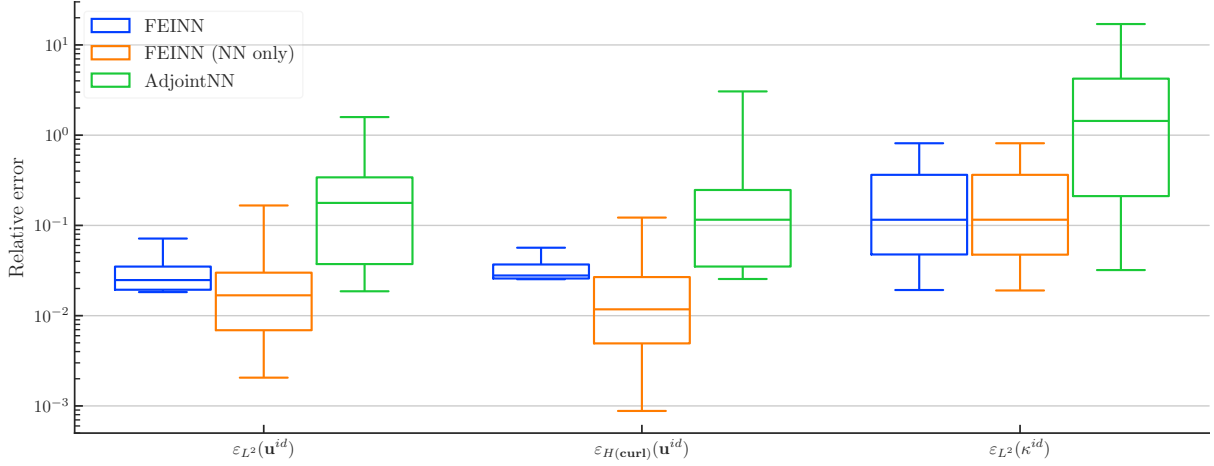


FIGURE 10. Comparison among FEINNs and adjoint NNs in terms of relative errors (depicted using box plots) with 100 different NN initialisations for the inverse Maxwell problem with partial observations.

state are the same as in Sect. 3.3.1, while the analytical coefficient is

$$\kappa(x, y) = \frac{1}{1 + x^2 + y^2 + (x - 1)^2 + (y - 1)^2}.$$

Regarding the NN structures, the only change is an increase in the number of neurons in  $\kappa_{\mathcal{N}}$  from 20 to 50. For compatible FEINNs, the training iterations are set to [150, 50,  $2 \times 400$ ], with penalty coefficients [0.01, 0.03]. The total training iterations for adjoint NNs are also set to 1,000.

We juxtapose the true solutions, non-interpolated NN solutions, and their corresponding errors in Fig. 11. Note that we use the same analytic state as in the previous experiment; therefore, instead of presenting the state itself, we depict its curl. Additionally, we observe that the NN solutions for the state consistently outperform their interpolations. Hence, we only present the non-interpolated NN solutions in the figure. Let us first discuss the state solutions. Since  $\mathbf{u}_{\mathcal{N}} \in C^\infty(\bar{\Omega})$ ,  $\nabla \times \mathbf{u}_{\mathcal{N}}$  is also smooth, as confirmed in Fig. 11b. However, upon interpolation onto an edge FE space with  $C^0$  normal components, we expect observing discontinuities at the element boundaries in the curl of the interpolated state solution, similar to those displayed in Fig. 4b. The smoothness of  $\mathbf{u}_{\mathcal{N}}$  enhances the accuracy of the state NN solutions in terms of curl error. In this experiment, the relative curl error of the interpolated  $u_{\mathcal{N}}$  is  $2.5 \times 10^{-2}$ , while  $u_{\mathcal{N}}$  itself achieves a lower relative curl error of  $1.5 \times 10^{-3}$ . For the coefficient, the NN solution (Fig. 11e) successfully identifies the pattern of the true coefficient (Fig. 11d), with the pointwise error (Fig. 11f) below 0.05 across most of the domain.

The training error histories of both FEINNs and adjoint NNs are presented in Fig. 12. The label tag “no reg” for the adjoint NN method denotes the history without regularisation. It is evident that, although the adjoint NN method converges faster than the FEINN method, it requires explicit regularisation to stabilise the training. We adopt the same  $L^1$  regularisation on the parameters of  $\kappa_{\mathcal{N}}$  as in [53], with a coefficient  $10^{-3}$ . One advantage of the FEINN method is that no regularisation is needed to achieve a stable training even though regularisation could help to make the problem better posed and improve convergence. Moreover, the non-interpolated NNs have the potential for better state accuracy due to the smoothness of  $\mathbf{u}_{\mathcal{N}}$ , as the errors of  $\mathbf{u}_{\mathcal{N}}$  fall below the adjoint NN errors after 300 iterations.

To study the robustness of the methods, we repeat the experiment 100 times with different NN initialisations. The resulting box plots for the relative errors are presented on the left side of Fig. 13. For the identified states, both FEINNs and adjoint NNs exhibit stable and similar performance, as evidenced by the boxes degenerating into lines and being positioned at the same level. However, the FEINN method has more potential than the adjoint NN method to achieve better accuracy, as the non-interpolated NN boxes are noticeably lower than the adjoint NN boxes. For the coefficient, the adjoint NN method is more stable than the FEINN method, with a more compact box plot. The FEINN method also yields highly accurate results: the upper quartile (Q3) line of the FEINN coefficient box is below 9%, and a similar trend is observed for NNs without interpolation. In summary, the FEINN method demonstrates comparable performance to

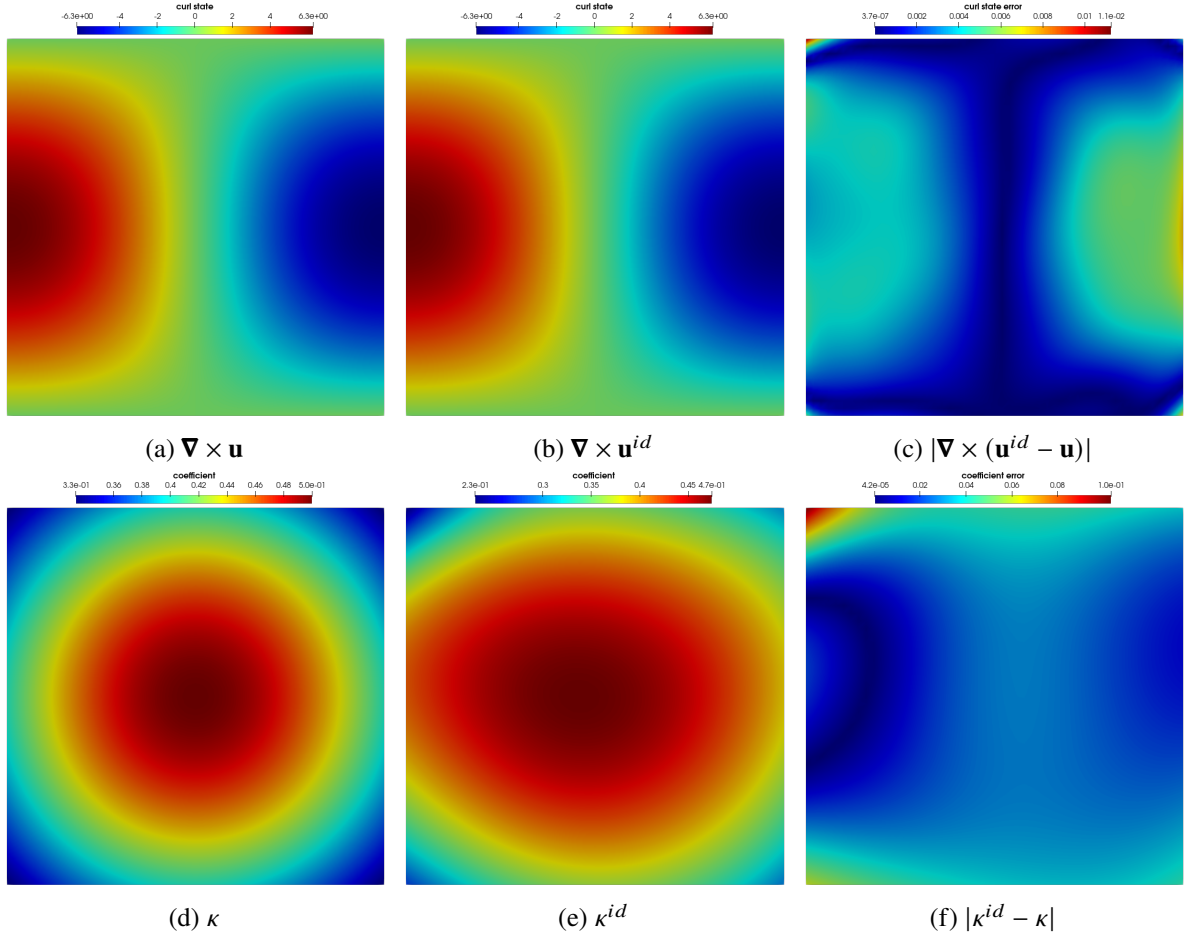


FIGURE 11. Illustration of known analytical solutions (first column), compatible FEINN solutions (second column), and corresponding point-wise errors (third column) for the inverse Maxwell problem with noisy observations. Results correspond to an experiment with a specific NN initialisation. The first row depicts the curl of the state, while the second row represents the coefficient.

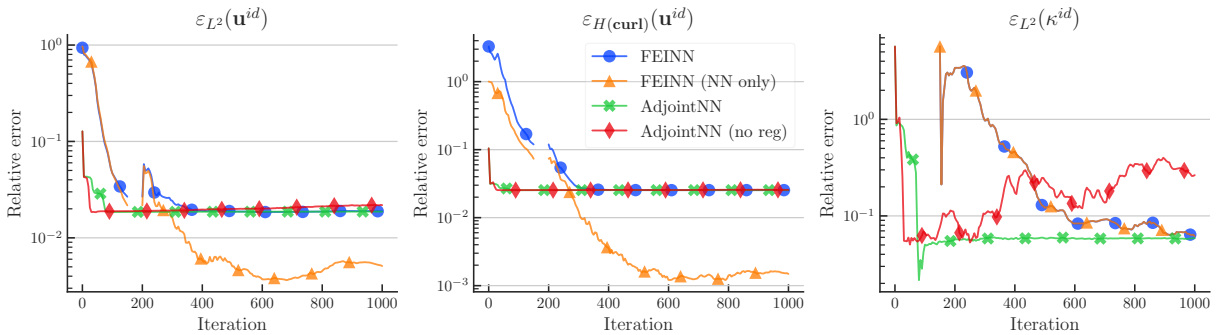


FIGURE 12. Comparison among FEINNs and adjoint NNs in terms of relative errors during training for the inverse Maxwell problem with noisy observations. Both optimisation loops were run for 1,000 iterations.

the adjoint NN method in identifying unknown coefficient, and it demonstrates greater potential in fully recovering the state with noisy data.

In addition to NN initialisations, another source of randomness in this problem is the Gaussian noise in the observations. To assess the sensitivity of FEINNs to this noise, we generate 100 different sets of noisy observations using different random seeds and repeat the experiment with the same set of NN initialisations.

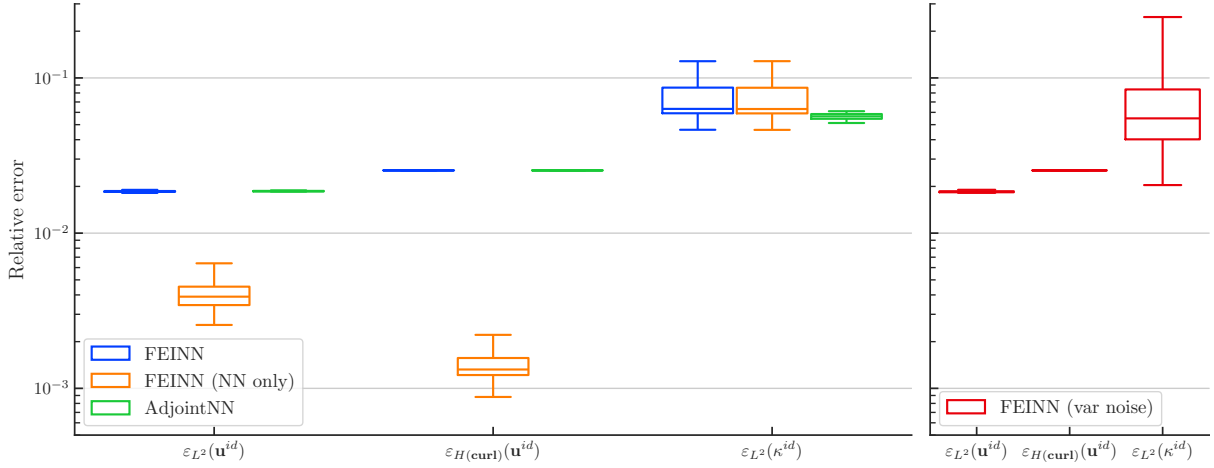


FIGURE 13. Box plots from 100 experiments for the inverse Maxwell problem with noisy observations. Left: comparison among FEINNs and adjoint NNs with regularisation in terms of relative errors with different NN initialisations. Right: sensitivity analysis of FEINNs to Gaussian noise in observations, generated using different random seeds.

The resulting box plots for the relative errors are displayed on the right side of Fig. 13, conforming the robustness of the FEINN method to random noise. The state boxes are mostly flat, while the Q3 value of the coefficient box remains below 9%.

3.3.3. *Boundary observations.* We conclude the inverse experiments section by attacking a boundary value inverse Maxwell problem. This scenario is particularly challenging as state observations are available only around the boundary, while the state in the interior domain is unknown. To add more complexity, we assume that the unknown coefficient  $\varepsilon \kappa$  is discontinuous across the domain  $\Omega = [0, 1]^2$ . The analytical solutions are as follows:

$$\mathbf{u}(x, y) = \begin{bmatrix} \cos(\pi x) \cos(y) \\ \sin(x) \sin(\pi y) \end{bmatrix}, \quad \kappa(x, y) = \begin{cases} 1, & \text{if } y > 2x \\ 10, & \text{if } y \leq 2x \end{cases}.$$

The curl of the analytic state and the discontinuous  $\kappa$  are depicted in Fig. 14a and Fig. 14d, respectively. A total of  $4 \times 70$  boundary observations are generated by evaluating the true state along the interior side of the boundary. Their locations are marked as purple dots in Fig. 14a.

In this experiment, we focus exclusively on the compatible FEINN approach. Since the Dirichlet boundary condition is presented as boundary observations, the interpolation space for  $\mathbf{u}_N$  is taken as  $U_h^1$  rather than  $U_{h,0}^1$  in the previous experiments. To reflect this change in the FE space, the loss (20) is modified as follows:

$$\mathcal{L}(\boldsymbol{\kappa}_N, \mathbf{u}_N) \doteq \|\mathbf{d} - \mathcal{D}_h(\pi_h^1(\mathbf{u}_N))\|_{\ell^2} + \alpha \|\tilde{\mathcal{R}}_h(\pi_h^0(\boldsymbol{\kappa}_N), \pi_h^1(\mathbf{u}_N))\|_{V^1},$$

where  $\tilde{\mathcal{R}}(\boldsymbol{\kappa}, \mathbf{u}, \mathbf{v}) = a(\boldsymbol{\kappa}, \mathbf{u}, \mathbf{v}) - \ell(\mathbf{v}) - \int_{\partial\Omega} (\mathbf{v} \times \mathbf{n}) \cdot (\nabla \times \mathbf{u})$  is the modified PDE residual. The boundary integral term in  $\tilde{\mathcal{R}}$  arises from integration by parts and the fact that  $\mathbf{v} \times \mathbf{n}$  is not necessarily zero on  $\partial\Omega$ .

The NN structures for  $\mathbf{u}_N$  and  $\boldsymbol{\kappa}_N$  remain the same as in the noisy observations experiment. The training iterations and penalty coefficients are set to  $[150, 50, 3 \times 400]$  and  $[0.001, 0.003, 0.009]$ , respectively. The mesh consist of  $100 \times 100$  squares, and the interpolation space orders are consistent with those in the earlier inverse experiments. We present the trained NN solutions and their errors in the last two columns of Fig. 14. Despite having state observations only around the boundary, the curl of the NN state solution produced by our method are visually indistinguishable from the curl of the true state, as evident from the comparison of Fig. 14b and Fig. 14a. Moreover, the identified NN coefficient as shown in Fig. 14e successfully captures the jumps of the true coefficient. The pointwise error of the coefficient, depicted in Fig. 14f, is small in most regions of the domain, with slightly higher errors near the discontinuity.

Fig. 15 illustrates the training error histories for the compatible FEINN method. All relative errors decrease steadily during training and converge to low levels. Additionally, after a few hundred iterations,  $\mathbf{u}_N$  errors consistently fall below those of its interpolation counterpart in both  $L^2$  and  $H(\mathbf{curl})$  norms. Overall,

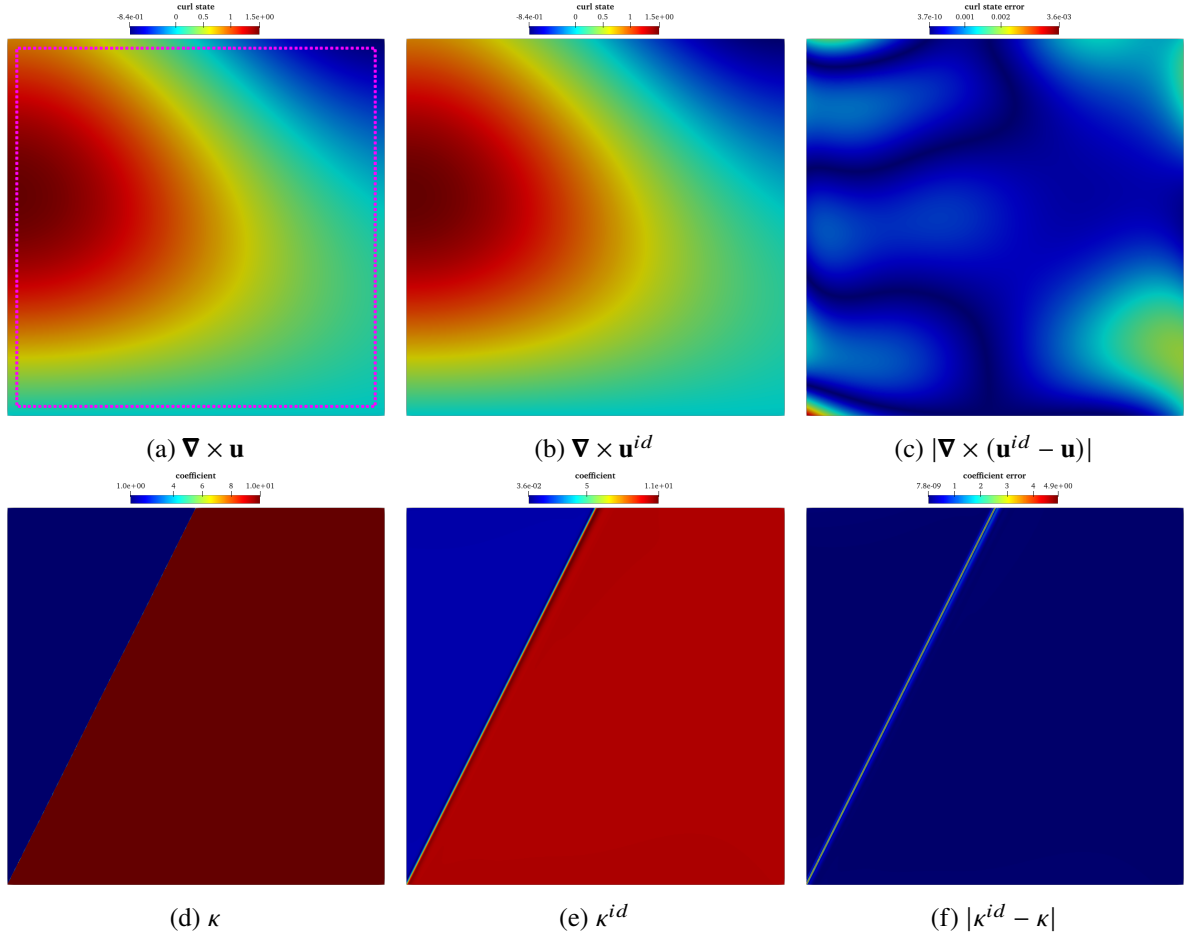


FIGURE 14. Illustration of analytical and NN solutions and the errors for the inverse Maxwell problem with boundary observations. The purple dots in (a) represent the observed data. See caption of Fig. 11 for details on the information being displayed in this figure.

the training curves confirm the reliability of our 3-step training strategy and the potential for  $\mathbf{u}_N$  to achieve higher accuracy than its FE interpolation when trained with boundary observations.

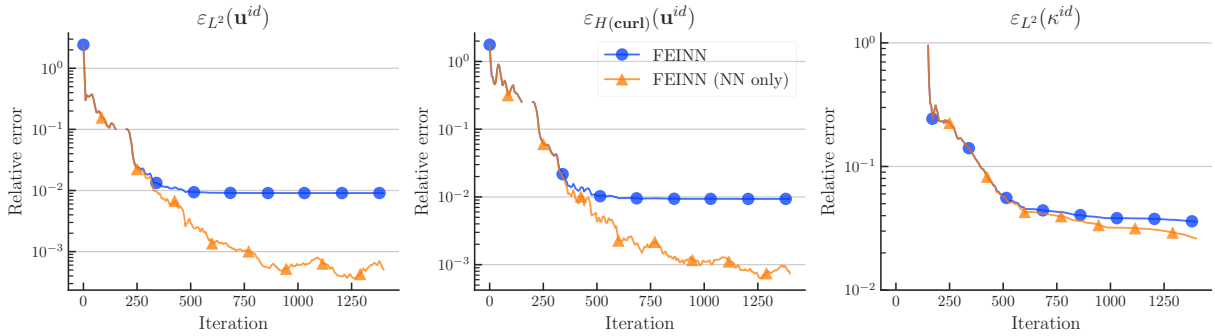


FIGURE 15. Relative errors during training by the compatible FEINN method for the inverse Maxwell problem with boundary observations.

Similar to previous experiments, we conduct 100 trials with different NN initial parameters to assess our method's robustness in the boundary observations case. The resulting box plots for the relative errors are presented in Fig. 16. For the state, the interpolated NNs are highly reliable and accurate, with line-like error boxes positioned at 1% relative errors in both  $L^2$  and  $H(\mathbf{curl})$  norms. Although non-interpolated NN solutions result in slightly more scattered boxes, they demonstrate greater accuracy than their

interpolation counterparts. This is reflected in the upper whisker lines for the  $L^2$  and  $H(\mathbf{curl})$  relative errors, which are below 0.2% and 0.3%, respectively. Regarding the coefficient, the NNs achieve a 1% error reduction compared to their interpolations, with most  $\kappa_{\mathcal{N}}$  errors around 3%. These coefficient error boxes are nearly flat, with an interquartile range of less than 1%. These results highlight our method’s robustness in recovering both the state and discontinuous coefficient of the inverse Maxwell problem using only boundary observations.

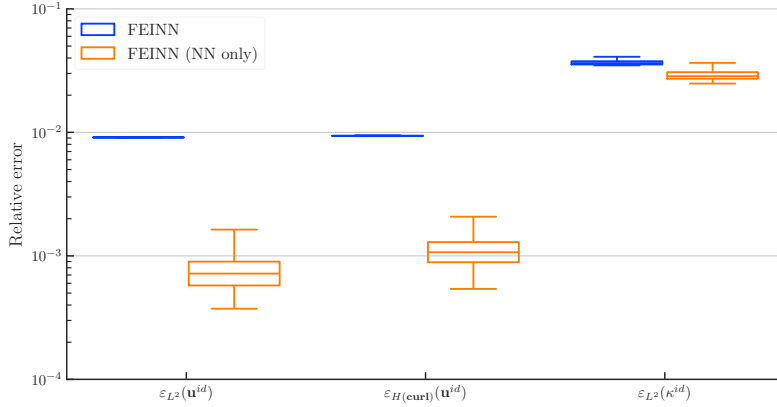


FIGURE 16. Box plots from 100 experiments for the inverse Maxwell problem with boundary observations.

#### 4. CONCLUSIONS

In this work, we extended the FEINN method [16] to solve vector-valued PDEs with weak solutions in  $H(\mathbf{curl})$  or  $H(\mathbf{div})$  spaces by interpolating NNs onto compatible FE spaces, i.e., structure-preserving spaces that satisfy a discrete de Rham subcomplex, such as Nédélec and RT spaces. We also propose an extension, trace FEINNs, to solve surface Darcy equations by interpolating NNs onto FE spaces defined on the discrete manifold. The compatible FEINN method retains the advantages of standard FEINNs, such as exact integration, seamless imposition of strong boundary conditions, and a solid mathematical foundation. Additionally, compatible FEINNs can be easily adapted to inverse problems by adding the data misfit error to the loss function and introducing new NNs to approximate the unknown physical coefficients.

To evaluate the performance of the methods, we conducted experiments on both forward and inverse problems. Specifically, in the forward Maxwell problem, we analysed how compatible FEINNs perform across different mesh sizes and trial FE space orders. To showcase the applicability of compatible FEINNs to surface PDEs, we tackled a forward Darcy problem on the unit sphere. In general, we observe that using lower-order test bases allows NNs to beat FEM solutions in terms of  $L^2$  and  $H(\mathbf{curl})$  errors for problems with a smooth analytic solution, achieving over two orders of magnitude improvement over FE solutions. In addition, interpolated NNs match the FE solutions in all cases. Preconditioning of NNs (i.e., using dual residual norms in the loss function) improves the stability and efficiency of the training process. Our findings also suggest that the strong PDE residual with NNs effectively guides mesh refinement during adaptive training, resulting in NNs that are more accurate than or comparable to FEM solutions. For inverse problems, we compare the compatible FEINN method with the adjoint NN method for the inverse Maxwell problem with partial or noisy observations. Compatible FEINNs are more accurate than adjoint NNs in most cases, do not require explicit regularisation and are robust against random noise in the observations. Besides, the FEINN method also achieves high accuracy in both state and coefficient for the inverse problem with boundary observations.

Even though FEINNs have been shown to be more accurate and stable than other PINN-like methods [16, 18], the cost of the training is still high. For forward problems, despite the gains in accuracy compared to FEM on the same mesh, computational cost is higher than FEMs with similar accuracy in general. Adaptive and inverse problems improve the efficiency of the method compared to standard approaches, since nested loops are not required and NN built-in regularisation can be exploited. We also expect these schemes to be more effective for transient simulations, where the NN can be initialised with the previous time step training.

In the future, the design of novel nonconvex optimisation strategies for NN approximation of PDEs, e.g., using multigrid and domain decomposition-like techniques, will be critical to reduce the computational cost of training of PINN-like strategies and efficiently exploit their nonlinear approximability properties.

## ACKNOWLEDGMENTS

This research was partially funded by the Australian Government through the Australian Research Council (project numbers DP210103092 and DP220103160). This work was also supported by computational resources provided by the Australian Government through NCI under the NCMAS and ANU Merit Allocation Schemes. W. Li gratefully acknowledges the Monash Graduate Scholarship from Monash University, the NCI computing resources provided by Monash eResearch through Monash NCI scheme for HPC services, and the support from the Laboratory for Turbulence Research in Aerospace and Combustion (LTRAC) at Monash University through the use of their HPC Clusters.

## DECLARATION OF GENERATIVE AI AND AI-ASSISTED TECHNOLOGIES IN THE WRITING PROCESS

During the preparation of this work the authors used ChatGPT in order to improve language and readability. After using this tool/service, the authors reviewed and edited the content as needed and take full responsibility for the content of the publication.

## REFERENCES

- [1] A. Ern and J.-L. Guermond. *Finite Elements I*. Springer International Publishing, 2021. DOI: [10.1007/978-3-030-56341-7](https://doi.org/10.1007/978-3-030-56341-7).
- [2] S. Badia, A. F. Martín, and J. Principe. “Multilevel Balancing Domain Decomposition at Extreme Scales”. In: *SIAM Journal on Scientific Computing* 38.1 (2016), pp. C22–C52. DOI: [10.1137/15M1013511](https://doi.org/10.1137/15M1013511).
- [3] D. N. Arnold, R. S. Falk, and R. Winther. “Finite element exterior calculus, homological techniques, and applications”. In: *Acta Numerica* 15 (2006), pp. 1–155. DOI: [10.1017/s0962492906210018](https://doi.org/10.1017/s0962492906210018).
- [4] C. J. Cotter. “Compatible finite element methods for geophysical fluid dynamics”. In: *Acta Numerica* 32 (2023), pp. 291–393. DOI: [10.1017/S0962492923000028](https://doi.org/10.1017/S0962492923000028).
- [5] J.-C. Nédélec. “Mixed finite elements in  $R^3$ ”. In: *Numerische Mathematik* 35.3 (Sept. 1980), pp. 315–341. DOI: [10.1007/BF01396415](https://doi.org/10.1007/BF01396415).
- [6] P. A. Raviart and J. M. Thomas. “A mixed finite element method for 2-nd order elliptic problems”. In: *Mathematical Aspects of Finite Element Methods*. Ed. by I. Galligani and E. Magenes. Berlin, Heidelberg: Springer Berlin Heidelberg, 1977, pp. 292–315. DOI: [10.1007/BFb0064470](https://doi.org/10.1007/BFb0064470).
- [7] M. Costabel and M. Dauge. “Weighted regularization of Maxwell equations in polyhedral domains”. In: *Numerische Mathematik* 93.2 (Dec. 2002), pp. 239–277.
- [8] P. Monk and Y. Zhang. “Finite Element Methods for Maxwell’s Equations”. In: *arXiv* (2019).
- [9] M. Raissi, P. Perdikaris, and G. Karniadakis. “Physics-informed neural networks: A deep learning framework for solving forward and inverse problems involving nonlinear partial differential equations”. In: *Journal of Computational Physics* 378 (2019), pp. 686–707. DOI: [10.1016/j.jcp.2018.10.045](https://doi.org/10.1016/j.jcp.2018.10.045).
- [10] G. Pang, L. Lu, and G. E. Karniadakis. “fPINNs: Fractional Physics-Informed Neural Networks”. In: *SIAM Journal on Scientific Computing* 41.4 (2019), A2603–A2626. DOI: [10.1137/18M1229845](https://doi.org/10.1137/18M1229845).
- [11] L. Yang, X. Meng, and G. E. Karniadakis. “B-PINNs: Bayesian physics-informed neural networks for forward and inverse PDE problems with noisy data”. In: *Journal of Computational Physics* 425 (2021), p. 109913. DOI: [10.1016/j.jcp.2020.109913](https://doi.org/10.1016/j.jcp.2020.109913).
- [12] E. Kharazmi, Z. Zhang, and G. E. Karniadakis. “hp-VPINNs: Variational physics-informed neural networks with domain decomposition”. In: *Computer Methods in Applied Mechanics and Engineering* 374 (2021), p. 113547. DOI: [10.1016/j.cma.2020.113547](https://doi.org/10.1016/j.cma.2020.113547).
- [13] A. Magueresse and S. Badia. “Adaptive quadratures for nonlinear approximation of low-dimensional PDEs using smooth neural networks”. In: *Computers & Mathematics with Applications* 162 (2024), pp. 1–21. DOI: [10.1016/j.camwa.2024.02.041](https://doi.org/10.1016/j.camwa.2024.02.041).
- [14] S. Berrone, C. Canuto, and M. Pintore. “Variational Physics Informed Neural Networks: the Role of Quadratures and Test Functions”. In: *Journal of Scientific Computing* 92.3 (Aug. 2022), p. 100. DOI: [10.1007/s10915-022-01950-4](https://doi.org/10.1007/s10915-022-01950-4).

- [15] N. Sukumar and A. Srivastava. “Exact imposition of boundary conditions with distance functions in physics-informed deep neural networks”. In: *Computer Methods in Applied Mechanics and Engineering* 389 (2022), p. 114333. DOI: [10.1016/j.cma.2021.114333](https://doi.org/10.1016/j.cma.2021.114333).
- [16] S. Badia, W. Li, and A. F. Martín. “Finite element interpolated neural networks for solving forward and inverse problems”. In: *Computer Methods in Applied Mechanics and Engineering* 418 (2024), p. 116505. DOI: [10.1016/j.cma.2023.116505](https://doi.org/10.1016/j.cma.2023.116505).
- [17] S. Rojas, P. Maczuga, J. Muñoz-Matute, D. Pardo, and M. Paszyński. “Robust variational physics-informed neural networks”. In: *Comput. Methods Appl. Mech. Eng.* 425 (116904 May 2024), p. 116904. DOI: [10.1016/j.cma.2024.116904](https://doi.org/10.1016/j.cma.2024.116904).
- [18] S. Badia, W. Li, and A. F. Martín. “Adaptive finite element interpolated neural networks”. In: *Computer Methods in Applied Mechanics and Engineering* 437 (2025), p. 117806. DOI: [10.1016/j.cma.2025.117806](https://doi.org/10.1016/j.cma.2025.117806).
- [19] S. Cai et al. “Flow over an espresso cup: inferring 3-D velocity and pressure fields from tomographic background oriented Schlieren via physics-informed neural networks”. In: *Journal of Fluid Mechanics* 915 (2021), A102. DOI: [10.1017/jfm.2021.135](https://doi.org/10.1017/jfm.2021.135).
- [20] C. Cheng and G.-T. Zhang. “Deep Learning Method Based on Physics Informed Neural Network with Resnet Block for Solving Fluid Flow Problems”. In: *Water* 13.4 (2021). DOI: [10.3390/w13040423](https://doi.org/10.3390/w13040423).
- [21] F. Pichi, F. Ballarin, G. Rozza, and J. S. Hesthaven. “An artificial neural network approach to bifurcating phenomena in computational fluid dynamics”. In: *Computers & Fluids* 254 (2023), p. 105813. DOI: [10.1016/j.compfluid.2023.105813](https://doi.org/10.1016/j.compfluid.2023.105813).
- [22] M. Baldan, G. Baldan, and B. Nacke. “Solving 1D non-linear magneto quasi-static Maxwell’s equations using neural networks”. In: *IET Science, Measurement & Technology* 15.2 (2021), pp. 204–217. DOI: [10.1049/smt2.12022](https://doi.org/10.1049/smt2.12022).
- [23] J. Lim and D. Psaltis. “MaxwellNet: Physics-driven deep neural network training based on Maxwell’s equations”. In: *APL Photonics* 7.1 (Jan. 2022), p. 011301. DOI: [10.1063/5.0071616](https://doi.org/10.1063/5.0071616).
- [24] M. Baldan, P. Di Barba, and D. A. Lowther. “Physics-Informed Neural Networks for Inverse Electromagnetic Problems”. In: *IEEE Transactions on Magnetics* 59.5 (2023), pp. 1–5. DOI: [10.1109/TMAG.2023.3247023](https://doi.org/10.1109/TMAG.2023.3247023).
- [25] Z. Zhang et al. “A physics-informed convolutional neural network for the simulation and prediction of two-phase Darcy flows in heterogeneous porous media”. In: *Journal of Computational Physics* 477 (2023), p. 111919. DOI: [10.1016/j.jcp.2023.111919](https://doi.org/10.1016/j.jcp.2023.111919).
- [26] Q. He, D. Barajas-Solano, G. Tartakovsky, and A. M. Tartakovsky. “Physics-informed neural networks for multiphysics data assimilation with application to subsurface transport”. In: *Advances in Water Resources* 141 (2020), p. 103610. DOI: [10.1016/j.advwatres.2020.103610](https://doi.org/10.1016/j.advwatres.2020.103610).
- [27] Z. Fang and J. Zhan. “A Physics-Informed Neural Network Framework for PDEs on 3D Surfaces: Time Independent Problems”. In: *IEEE Access* 8 (2020), pp. 26328–26335.
- [28] W.-F. Hu, Y.-J. Shih, T.-S. Lin, and M.-C. Lai. “A shallow physics-informed neural network for solving partial differential equations on static and evolving surfaces”. In: *Computer Methods in Applied Mechanics and Engineering* 418 (2024), p. 116486. DOI: [10.1016/j.cma.2023.116486](https://doi.org/10.1016/j.cma.2023.116486).
- [29] A. Bihlo and R. O. Popovych. “Physics-informed neural networks for the shallow-water equations on the sphere”. In: *Journal of Computational Physics* 456 (2022), p. 111024. DOI: [10.1016/j.jcp.2022.111024](https://doi.org/10.1016/j.jcp.2022.111024).
- [30] M. A. Olshanskii and A. Reusken. “Trace Finite Element Methods for PDEs on Surfaces”. In: *Geometrically Unfitted Finite Element Methods and Applications*. Ed. by S. P. A. Bordas, E. Burman, M. G. Larson, and M. A. Olshanskii. Cham: Springer International Publishing, 2017, pp. 211–258.
- [31] A. Ern and J.-L. Guermond. *Finite Elements II*. Springer International Publishing, 2021. DOI: [10.1007/978-3-030-56923-5](https://doi.org/10.1007/978-3-030-56923-5).
- [32] M. Olm, S. Badia, and A. F. Martín. “On a general implementation of h- and p-adaptive curl-conforming finite elements”. In: *Advances in Engineering Software* 132 (2019), pp. 74–91. DOI: [10.1016/j.advengsoft.2019.03.006](https://doi.org/10.1016/j.advengsoft.2019.03.006).
- [33] D. N. Arnold. *Finite Element Exterior Calculus*. CBMS-NSF Regional Conference Series in Applied Mathematics. New York, NY: Society for Industrial & Applied Mathematics, Jan. 30, 2019. DOI: [10.1137/1.9781611975543](https://doi.org/10.1137/1.9781611975543).

- [34] C. Ronchi, R. Iacono, and P. Paolucci. “The ‘‘Cubed Sphere’’: A New Method for the Solution of Partial Differential Equations in Spherical Geometry’’. In: *Journal of Computational Physics* 124.1 (1996), pp. 93–114. DOI: [10.1006/jcph.1996.0047](https://doi.org/10.1006/jcph.1996.0047).
- [35] M. E. Rognes, D. A. Ham, C. J. Cotter, and A. T. T. McRae. “Automating the solution of PDEs on the sphere and other manifolds in FEniCS 1.2’’. In: *Geoscientific Model Development* 6.6 (2013), pp. 2099–2119. DOI: [10.5194/gmd-6-2099-2013](https://doi.org/10.5194/gmd-6-2099-2013).
- [36] J. A. Rivera, J. M. Taylor, Á. J. Omella, and D. Pardo. “On quadrature rules for solving Partial Differential Equations using Neural Networks’’. In: *Computer Methods in Applied Mechanics and Engineering* 393 (2022), p. 114710. DOI: [10.1016/j.cma.2022.114710](https://doi.org/10.1016/j.cma.2022.114710).
- [37] R. Hiptmair and J. Xu. “Nodal auxiliary space preconditioning in  $H(\text{curl})$  and  $H(\text{div})$  spaces’’. In: *SIAM J. Numer. Anal.* 45 (6 Jan. 2007), pp. 2483–2509. DOI: [10.1137/060660588](https://doi.org/10.1137/060660588).
- [38] S. Badia and R. Codina. “A nodal-based finite element approximation of the Maxwell problem suitable for singular solutions’’. In: *SIAM J. Numer. Anal.* 50 (2 Jan. 2012), pp. 398–417. DOI: [10.1137/110835360](https://doi.org/10.1137/110835360).
- [39] S. Badia and R. Codina. “Unified stabilized finite element formulations for the stokes and the Darcy problems’’. In: *SIAM J. Numer. Anal.* 47 (3 Jan. 2009), pp. 1971–2000. DOI: [10.1137/08072632x](https://doi.org/10.1137/08072632x).
- [40] S. Badia and F. Verdugo. “Gridap: An extensible Finite Element toolbox in Julia’’. In: *Journal of Open Source Software* 5.52 (2020), p. 2520. DOI: [10.21105/joss.02520](https://doi.org/10.21105/joss.02520).
- [41] F. Verdugo and S. Badia. “The software design of Gridap: A Finite Element package based on the Julia JIT compiler’’. In: *Computer Physics Communications* 276 (July 2022), p. 108341. DOI: [10.1016/j.cpc.2022.108341](https://doi.org/10.1016/j.cpc.2022.108341).
- [42] M. Innes. “Flux: Elegant machine learning with Julia’’. In: *Journal of Open Source Software* 3.25 (2018), p. 602. DOI: [10.21105/joss.00602](https://doi.org/10.21105/joss.00602).
- [43] F. White et al. *JuliaDiff/ChainRules.jl: v1.69.0*. Version v1.69.0. June 2024. DOI: [10.5281/zenodo.11545120](https://doi.org/10.5281/zenodo.11545120).
- [44] A. F. Martín. *GridapP4est.jl*. 2024. URL: <https://github.com/gridap/GridapP4est.jl> (visited on 06/19/2024).
- [45] S. Badia, A. F. Martín, E. Neiva, and F. Verdugo. “A Generic Finite Element Framework on Parallel Tree-Based Adaptive Meshes’’. In: *SIAM Journal on Scientific Computing* 42.6 (2020), pp. C436–C468. DOI: [10.1137/20M1328786](https://doi.org/10.1137/20M1328786).
- [46] X. Glorot and Y. Bengio. “Understanding the difficulty of training deep feedforward neural networks’’. In: *Proceedings of the Thirteenth International Conference on Artificial Intelligence and Statistics*. Ed. by Y. W. Teh and M. Titterton. Vol. 9. Proceedings of Machine Learning Research. Chia Laguna Resort, Sardinia, Italy: PMLR, May 2010, pp. 249–256.
- [47] P. K. Mogensen and A. N. Riseth. “Optim: A mathematical optimization package for Julia’’. In: *Journal of Open Source Software* 3.24 (2018), p. 615. DOI: [10.21105/joss.00615](https://doi.org/10.21105/joss.00615).
- [48] R. Hiptmair. “Multigrid Method for Maxwell’s Equations’’. In: *SIAM Journal on Numerical Analysis* 36.1 (1998), pp. 204–225. DOI: [10.1137/S0036142997326203](https://doi.org/10.1137/S0036142997326203).
- [49] A. F. Martín. *GridapGeosciences.jl: Gridap drivers for geoscience applications*. 2024. URL: <https://github.com/gridapapps/GridapGeosciences.jl> (visited on 06/17/2024).
- [50] D. Lee, A. F. Martín, C. Bladwell, and S. Badia. “A comparison of variational upwinding schemes for geophysical fluids, and their application to potential enstrophy conserving discretisations’’. In: *Computers & Mathematics with Applications* 165 (2024), pp. 150–162. DOI: [10.1016/j.camwa.2024.04.016](https://doi.org/10.1016/j.camwa.2024.04.016).
- [51] C. Dong, C. C. Loy, K. He, and X. Tang. “Learning a Deep Convolutional Network for Image Super-Resolution’’. In: *Computer Vision – ECCV 2014*. Ed. by D. Fleet, T. Pajdla, B. Schiele, and T. Tuytelaars. Cham: Springer International Publishing, 2014, pp. 184–199.
- [52] J. Berg and K. Nyström. “Neural networks as smooth priors for inverse problems for PDEs’’. In: *Journal of Computational Mathematics and Data Science* 1 (2021), p. 100008. DOI: [10.1016/j.jcmds.2021.100008](https://doi.org/10.1016/j.jcmds.2021.100008).
- [53] S. K. Mitusch, S. W. Funke, and M. Kuchta. “Hybrid FEM-NN models: Combining artificial neural networks with the finite element method’’. In: *Journal of Computational Physics* 446 (2021), p. 110651. DOI: [10.1016/j.jcp.2021.110651](https://doi.org/10.1016/j.jcp.2021.110651).

- [54] A. A. Oberai, N. H. Gokhale, and G. R. Feijóo. “Solution of inverse problems in elasticity imaging using the adjoint method”. In: *Inverse Problems* 19.2 (Feb. 2003), p. 297. doi: [10.1088/0266-5611/19/2/304](https://doi.org/10.1088/0266-5611/19/2/304).